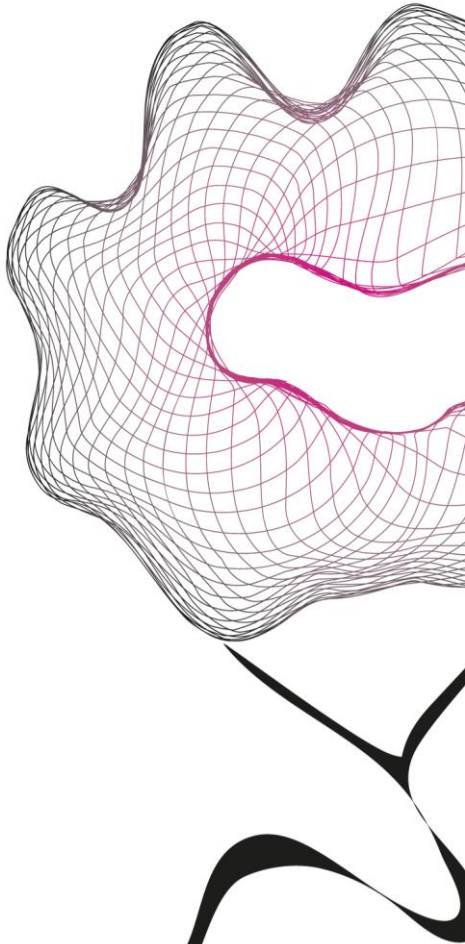


MASTER THESIS



MULTIPHOTON MICROSCOPY FOR IN- TISSUE IMAGING OF MICRO-ROBOTS

Ihar Hlukhau

FACULTY OF ENGINEERING TECHNOLOGY
DEPARTMENT OF BIOMECHANICAL ENGINEERING

EXAMINATION COMMITTEE

prof.dr. S. Misra
dr. L. Capuano
dr.ir. M. Abayazid

DOCUMENT NUMBER
BE - 855

Abstract

Micro-robots are miniaturized micro-scale (in-)organic agents of varying structure which are designed for minimally-invasive surgical applications, namely, micro-biopsy, tissue heating/penetration and intracellular delivery. These agents travel through complex and narrow pathways and encounter biological barriers (e.g., protein corona, immune attack, intratumoral pressure) imposed by the human body to protect itself from intruders. Navigation in such an environment requires a robust control strategy. Medical imaging provides position feedback in a closed-loop micro-robot control. The multiphoton fluorescence imaging is a technique of a particular interest that offers outstanding resolution capabilities. To the best of our knowledge, there is no research done targeting the imaging applications of it within surgical robotics. For that reason, the aim of this thesis is to prove the micro-robots imaging ability of a multiphoton system.

The software and hardware control algorithms were designed and implemented in an optical setup. Custom graphical user interface (GUI) allows for flexible control over the imaging parameters. Experiments with several types of tissues from rat and chicken were performed using miniaturized agents for single (size of $\approx 500 \mu\text{m}$) and swarm (head size of up to $25 \mu\text{m}$) imaging. The results show the penetration depth of $750 \mu\text{m}$ for a single-bot and $250 \mu\text{m}$ for a swarm imaging, with a possibility to reach even further.

Contents

Abstract	i
List of Abbreviations	iv
1 Introduction	1
1.1 Micro-robotics surgeries	1
1.2 Problem definition and research objective	1
1.3 Outline	1
2 Theoretical background	2
2.1 Fluorescence	2
2.2 Light source	3
2.3 Fluorescent microscopy	4
2.3.1 Scanning	4
2.3.2 Sensing	5
2.3.3 Noise	5
2.4 Tissue own fluorescence	5
2.5 Summary	5
3 State of the art	7
3.1 Micro-robots imaging	7
3.1.1 Magnetic	7
3.1.2 Ultrasound	8
3.1.3 Ionizing Radiation	8
3.1.4 Optical	9
3.1.5 Hybrid	10
3.2 Multiphoton fluorescence imaging	10
3.3 Discussion	11
4 Multiphoton imaging setup	13
4.1 Hardware	13
4.2 Software	14
4.2.1 General architecture	14
4.2.2 Image Acquisition	14
4.2.3 Image Processing	15
4.2.4 Software Performance	16
4.2.5 Software Interaction	16
5 Results and discussion	18
5.1 Materials and methods	18
5.2 Evaluation criteria	18
5.3 Single-bot imaging	19
5.4 Swarm imaging	20
5.5 Discussion	20
5.6 Frame averaging	22
6 Conclusions	23
6.1 Achieved goals	23
6.2 Future work	23
6.2.1 Hardware	23
6.2.2 Software	23
Bibliography	24

A Additional material **27**

A.1 Steering algorithm 27

A.2 Mouse liver swarm imaging 27

List of Abbreviations

MPM	multi-photon microscopy
IR	infrared
TPEF	two-photon excitation fluorescence
SHG	second harmonic generation
2P	two-photon
3P	three-photon
SNR	signal-to-noise ratio
MRI	magnetic resonance imaging
MPI	magnetic particle imaging
OCT	optical coherence tomography
PAI	photo-acoustic imaging
MMUS	magnetomotive ultrasound imaging
CT	computed tomography
PET	positron emission tomography
SPECT	single photon emission computed tomography
MP-fi	multiphoton femto-imaging
RTC	real-time control
DAQ	data acquisition
PMT	photo-multiplier tube
GUI	graphical user interface
NA	numerical aperture
2D	two-dimensional
3D	three-dimensional
FOV	field of view
FLIM	fluorescence lifetime imaging

Chapter 1. Introduction

1.1 Micro-robotics surgeries

Surgeries are typically invasive, requiring a lot of manipulations of the tissues, especially if the target area is located at deep remote region. This causes damage to the patient, including bleeding and post-surgery complications. To address this issues, new minimally invasive techniques are being developed. Recent research is focused on the employment of miniaturized agents utilizing the remote control and imaging for navigation. Such minimum intervention procedures result in less tissue damage and consequently lower chance of complications and faster recovery time [1].

Due to the small size of micro-robots and wireless mobility, these can reach small, complex and hard-to-reach areas in human body to perform diverse medical procedures [1–4]. New ways on use of micro-robots in precision medicine are constantly appearing. Potential uses are minimally invasive surgeries, targeted drug delivery, sensing and diagnosis [1–5].

1.2 Problem definition and research objective

In order for the micro-robots to operate in the challenging environment of a human body, robust control is required. This is only possible, if the precise position of the micro-robot is known. A medical imaging technology should be used to perform this tracking. There are a variety of imaging methods, these will be discussed in Chapter 3, however the clinically-relevant imaging is still an ongoing challenge as most current methods are not up to par with the clinical standards.

Multiphoton fluorescence imaging is a light-based imaging technique able to provide an extremely high spatial resolution. In a current research, its main purpose is visualization of structures and processes within living organisms for the purpose of clinical diagnosis or biological research. To the best of our knowledge, no one presented its application for micro-robots imaging.

This research explores the feasibility of using multiphoton fluorescence imaging for micro-robots imaging. Based on this, the research objectives are formulated as follows: (1) Is it possible to image micro-robots using the multiphoton absorption process? (2) How well does this technique perform in terms of spatial resolution and imaging depth? (3) Can the micro-robots be imaged simultaneously with their surrounding structures? To answer these research questions, a custom multiphoton imaging setup was built with the focus of this thesis on the main algorithm for software and hardware control of the system. Using animal tissues, we are able to provide experimental evidence that micro-robots can indeed be imaged through various tissues.

1.3 Outline

In Chapter 2, a theoretical foundation is presented, introducing multiphoton absorption process and multi-photon microscopy (MPM). Chapter 3 provides an overview of modern micro-robots imaging techniques and reviews the state of the art of MPM. The hardware and software architecture of the MPM setup are described in Chapter 4; design choices and implementation are discussed. Experimental results and their discussions are presented in Chapter 5. Lastly, Chapter 6 sums up the research, provides a feedback on the progress and introduces several ideas for the future work.

Chapter 2. Theoretical background

This chapter presents fundamental concepts which are aimed at helping the reader to understand the following chapters. It explains the mechanics of fluorescence generation (section 2.1), light source characteristics (section 2.2), implementation of a fluorescence imaging system (section 2.3) and the natural fluorescence sources present in tissues (section 2.4). Lastly, the multiphoton fluorescence imaging theory is summarized in section 2.5.

2.1 Fluorescence

Fluorescence is the process of absorption and re-emission of light (i.e. one or multiple photons) by a molecule [6]. To understand this process, a general idea about the absorption and emission mechanism has to be discussed.

There exist two bands, which describe electrons' energy levels. The valence band, containing all of the potentially excitable electrons, and the conduction band, containing the excited electrons which have moved from the valence band [7]. Bandgap is the energy range in-between, where no electron states can exist. In order for an electron to move from the valence to the conduction band, external energy should be applied. This energy should be higher than that of the band gap [7]. In our case, the energy comes from the photons.

Linear fluorescence is triggered by a single photon, which is absorbed by an electron. Provided enough energy, the electron gets excited, causing it to "jump" from the valence to the conduction band, as shown on Fig. 2.1(a). This state is unstable and lasts very short time – in order of few nanoseconds. Afterwards, the excited electron falls back to the conduction band, releasing a photon. The energy of the emitted photon is nearly equal to the exciting photon, except for small losses. [6, 7].

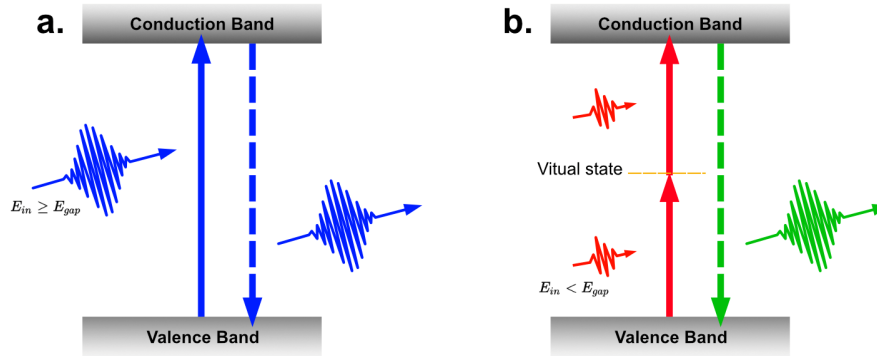


Figure 2.1: Fluorescence with one- and two-photon excitation. **a.** Because the absorbed single photon energy exceeds the band gap, the electron jumps to the conduction band. A single photon with identical energy is released back. **b.** Electron jumps to the conduction band through virtual state, absorbing two photons with a combined energy higher than the bandgap. A single photon with an energy equal as the bandgap is released back. Adapted from [8].

To trigger the fluorescence with multiple photons, the energy comes from multiple sources, meaning two or more photons have to be absorbed simultaneously. The simultaneous event is often referred to a time interval that lasts less than 10^{-16} seconds according to [7, 9] or less than 10^{-18} seconds according to [6, 10]. With two-photon (2P) absorption, two photons having at least half the energy of the band gap can excite the electron through a virtual state, as shown on Fig. 2.1(b). Upon falling back to the valence band, only one photon is emitted back having the same energy as the bandgap. According to (2.1), the energy (E) and the wavelength (λ) have inverse relation, indicating that emitted photon has half the wavelength [6, 7]. These phenomena allow for the use of shorter wavelength light sources for fluorescence imaging, which has various advantages that will be addressed in the following sections.

$$E = \frac{hc}{\lambda} \quad (2.1)$$

2.2 Light source

In order for an electron to absorb multiple photons, high photon fluxes in the range of 10^{20} – 10^{30} photons/($\text{cm}^2 \text{ s}$) are necessary. Under normal arc lamp illumination the probability to observe such an interaction is practically zero [6]. As follows from equation (2.2), the probability (P) of absorbing n photons is proportional to the probability of finding n photons within the volume it occupies in a given time period [7]. Such huge amount of photons requires accordingly high light intensity.

$$P_n = \left(\frac{m^n}{n!} \right) e^{-m} \quad (2.2)$$

Although extremely high power is required, the non-linear excitation relationship gives a particular advantage to the multiphoton excitation. The relation in (2.3) states the following: the probability (P) of two photon absorption is proportional to the square of the instantaneous laser intensity (irradiance I) [6, 7, 10]. This implies that absorption happens only near the focal volume where the peak intensity is high enough [8].

$$P \propto I^2 \quad (2.3)$$

The probability of excitation rapidly decreases outside the focal spot as the emission radiance decreases by a power of four from the focal point [6, 7]. Therefore, the fluorophore excitation is extremely precise. Outside the focal point, the photon density is too low and does not trigger the multiphoton absorption. The precision can be further modified by varying the focusing lenses. Using higher numerical aperture (NA) lenses, the focal volume decreases (Fig. 2.2(a)).

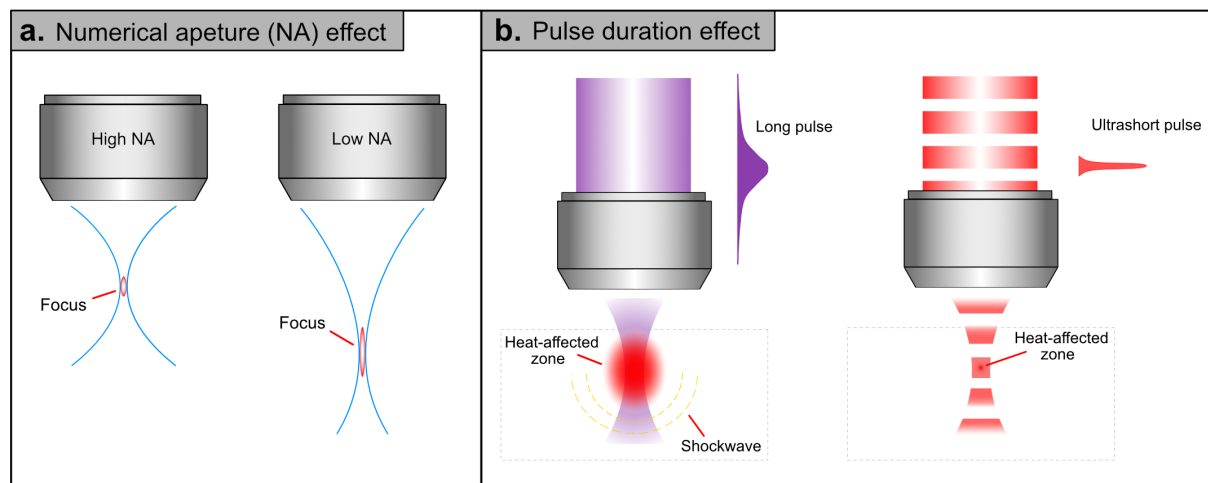


Figure 2.2: Effects of NA and pulse duration on the focal volume and the material interaction. **a.** High NA lens produces smaller focal volume comparing to a low NA lens but the focus is shallower. **b.** The long pulse causes the heat to spread and damage the tissue, resulting in shock waves. In comparison, the femtosecond pulses are extremely short lasting, preventing most of the heat damaging effect. Adapted from [8].

Delivering a pulse with enough intensity to trigger the multiphoton absorption at the specimen without simultaneously vaporizing it is a challenge. Hence, high frequency (high pulse repetition rate) lasers are employed to minimize the damage caused by the heating. The laser power can be described in two ways – instantaneous (peak) and average power. As goes from equation (2.4), there are two ways of increasing laser's power (P): increasing the number of photons (energy E) or condensing the photons into a smaller timed (t) pulse. This way, the peak power can reach megawatt values. To keep the average power low (in order of tens of milliwatts), the time duration in-between those pulses is 10^5 -fold longer than the pulse [6, 10].

$$P = \frac{E}{t} \quad (2.4)$$

For that purpose, multiphoton imaging relies on the femtosecond pulsed lasers, with pulse duration typically ranging from tens to hundreds of femtoseconds ($100 \text{ fs} = 10^{-13} \text{ s}$). As was mentioned, the fluorophore absorption event lasts nearly 10^{-18} seconds, meaning the pulse duration is relatively long and provide enough time for the fluorescence to appear. In addition, such a short pulse reduces the heat effect on tissues comparing to a long pulsed laser, as shown in Fig. 2.2(b). The reason is that most of the energy associated with the pulse is deposited into electrons before being transferred to the external structure [8, 11].

The lasers typically used for 2P excitation are Ti:Sapphire with a near-infrared (IR) wavelength, ranging between 700 and 1000 nm [9–12]. Near-IR light is shown to have much better tissue penetration then the light of any other wavelength. In addition, comparing to the shorter wavelength light, cell damaging aspect is decreased [10, 13, 14].

Despite mentioned benefits of the multiphoton light source, the hazard aspect still remains. Although the near-IR light is the least damaging spectrum of light to the tissues, an intensity of $> 250 \text{ mW}/\mu\text{m}^2$ and fluence of $> 0.3125 \text{ J}/\text{cm}^2$ (derived from [15]) may result in tissue damage. There are also specific limitations that arise from interaction with chromophores in the sample. As example, near infrared light is absorbed by the photosynthetic complex, while the melanin pigment can limit tissue imaging by causing thermal and mechanical damage during an experiment [6]. The dyes/fluorophores can also experience photobleaching proportional to the intensity of the laser. High concentration of photons in a very small volume accelerate the photobleaching effect, permanently disabling the molecules from emitting fluorescence [6].

2.3 Fluorescent microscopy

Fluorescent microscopy is a technique for acquiring microscopic images of materials by measuring the fluorescence of the imaging object at multiple spots [13].

2.3.1 Scanning

In order to create a digital image, it is necessary to scan an area using a beam of ultrashort pulsed laser light. For that, laser microscopy systems are used (Fig. 2.3). Galvanometric scanning system (usually referred as galvo) is widely used scanning mechanism because of its accuracy. Two mirrors rotate in perpendicular to deflect the beam and provide excitation light across the specimen [6, 14, 16]. Raster pattern is the most popular scanning approach, which includes two methods: uni- and bi-directional. In bi-directional method the galvo scans forward and backward (meaning after the galvo finished the image scan, instead of moving the focus back to the top-left corner of the scan area, it performs the scan from the bottom right corner in a backward direction). However, the torque for the galvo is not exactly the same for forward and backward scan, resulting in image aliasing. In addition, more computational power is required to form an image. The only benefit over uni-direction scan it has is less delay between scan cycles, which typically does not out-weight its disadvantages [16].

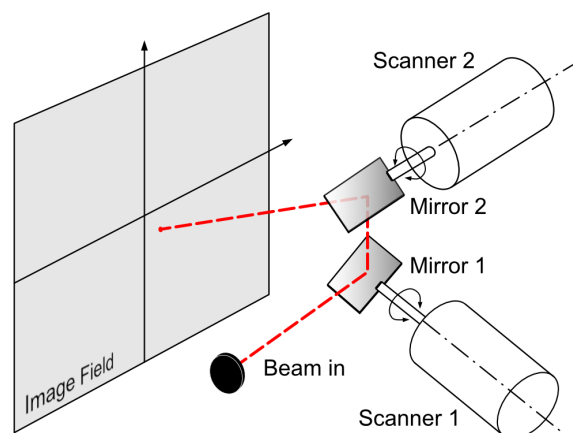


Figure 2.3: Laser scanning system. By steering the incoming beam with two parallel mirrors attached to the motors, the laser moves across the image field. Adapted from [17].

2.3.2 Sensing

The fluorescent signal is collected by a fast light-sensitive sensor. In order to read only the energy of specific wavelength, as the residual light might be present, an optical filter (wavelength-sensitive dichroic) is placed before the sensor, passing only the wavelength of interest (light coming from the fluorescence emission) [13, 14, 18]. There are two ways of collecting the light – whole-field and point-to-point. Whole-field sensors, such as CCD camera, collects the data from the entire imaging plane and cannot be used for MPM, which is based on a point-wise acquisition. Therefore, a point-to-point sensor called photo-multiplier tube (PMT) is often used. The output of the PMT is correlated to the number of detected photons, which shows the local concentration of fluorophores [18]. By processing the excitation information at different spots, the image is constructed. The pixels represent the spot area in a specific location of the specimen.

2.3.3 Noise

For correct utilization of the fluorescent microscopy, it is necessary to understand and reduce the errors in measurements. As error (noise) decreases relatively to the signal, measurement is getting more precise. In other words – the precision is limited by a signal-to-noise ratio (SNR) of the image.

The two most common types of noise are background noise and Poisson noise (also referred as shot noise) [18]. Background noise is the fluorescent signal that comes from non-target molecules which are natively present in tissues. Those are discussed in section 2.4. A common source of background noise is out-of-focus fluorescence, usually related to a size of the focal volume. Shot noise is connected to the nature of photons measurement, which has an intrinsic statistical uncertainty. Other sources can be thermal noise and non-perfect isolation (light coming from outside of the system). Important consideration is that detectors have limited capacity to hold electrons which results in pixel saturation, degrading the quality of the final image.

Noise is not constant and cannot be subtracted. However, if multiple images are collected and averaged together – the noise can be reduced. Averaging can be problematic for highly dynamic environments resulting in blur [18].

2.4 Tissue own fluorescence

Fluorescence can originate from the molecules originally present in tissues, allowing for imaging of body's internal structures by means of MPM. There are two mechanisms making it possible: autofluorescence and second harmonic generation (SHG).

The SHG occurs in non-symmetric molecules (mostly collagen for tissues) when excited with high-intensity short-pulsed light [9, 11]. The photons are not absorbed by the molecule but rather simultaneously scattered, combining and generating a single photon with combined energy [6, 19].

Autofluorescence is a phenomenon of emission of UV-visible and near-IR light by biomolecules natively present in tissues when excited by light at certain wavelength [20]. In our case the autofluorescence is caused by 2P excitation process and called two-photon excitation fluorescence (TPEF).

Different molecules found in tissues that emit fluorescence upon 2P near-IR excitation (700-1000 nm) include elastin, flavins, keratin, lipofuscin, collagen, etc. [9, 12, 15, 20]. Primary source of autofluorescence signal comes from NAD(P)H and flavins (located in cell cytoplasm) [20], while SHG primarily comes from collagen (located in skin and connective tissue) [9, 12].

Literature presents varying excitation wavelengths for these molecules, but it is generally accepted that an increase of wavelength makes fluorescence intensity decline. Action cross section (absorption cross section multiplied by the fluorescence quantum yield) value indicates the absorption rates of the photons in 2P process. Fig. 2.4(a) shows that action cross section drops for the shown molecules reaching the 1000 nm wavelength. The emission spectrum for the majority of intrinsic fluorescence in 2P excitation fall into 440 to 500 nm range (Fig. 2.4(b)).

2.5 Summary

To summarize, the MPM is a light-based medical imaging technology that involves scanning a tissue area, activating molecules along the beam path, and detecting the fluorescence generated at predetermined intervals. Based on these measurements, an image is constructed. The distinctive feature of the MPM is

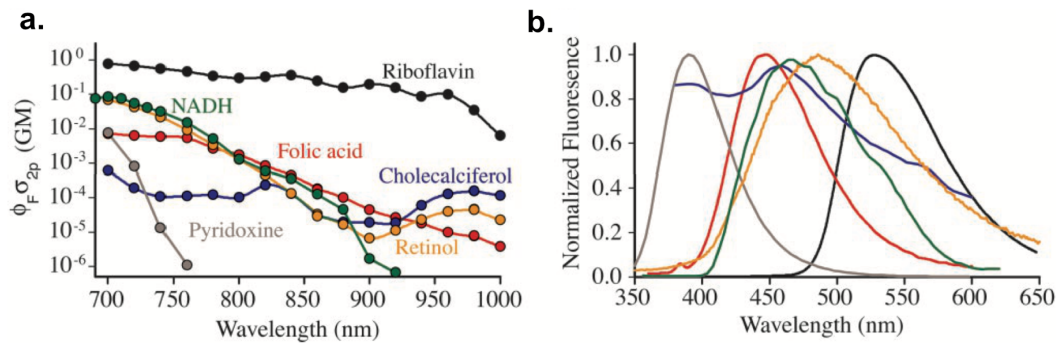


Figure 2.4: Tissue intrinsic fluorescence excitation and emission wavelength. **a.** Action cross section of molecules causing most of the intracellular TPEF. **b.** Emission spectra of the same molecules.

utilization of ultrashort near-IR pulsed laser allowing for high enough light intensity generation to trigger the multiphoton absorption. The advantages MPM provides are:

- **Reduced thermal effects.** The use of femtosecond laser significantly reduces thermal damage on the tissues as the time for an energy transfer to external structure is too short.
- **Micron resolution.** Having quadratic excitation dependency and almost no out-of-focus absorption, the excitation point is reduced to an extremely small volume.
- **Three-dimensional excitation control.** Resulting from the high resolution and the shape of the focal area, the excitation can be controlled over the three-dimensional (3D) space.
- **Deeper penetration and reduced photodamage.** The near-IR light used in MPM yields the best tissue penetration ability and reduced cell damage.
- **Imaging of the environment.** Due to tissue own fluorescence, the surrounding structures can be imaged through multiphoton excitation or SHG.

The limitations of MPM arise from the source intensity:

- **Accelerated photobleaching and photodamage at focal spot.** Laser intensity required for multiphoton absorption may permanently unable the molecules from emitting fluorescence or even cause thermal or mechanical damage to the tissue.

Chapter 3. State of the art

In order to determine the performance and feasibility of suggested technique for micro-robots imaging, the existing methods used for this function should be analyzed. The novel MPM setups are reviewed and conclusions on the relevance of the technique for micro-robots imaging are made.

3.1 Micro-robots imaging

All imaging techniques rely on the same principle – when energy is passed to a tissue, it gets absorbed or reflected, generating certain response signals. These signals are detected with corresponding sensors and processed into an image. Analyzing various image characteristics, the micro-robots can be localized [2, 5].

Imaging modalities can be categorized according to the underlying physics and include: (1) magnetic field, (2) ultrasound, (3) ionizing radiation and (4) optical-based [2–5]. In order to compare these modalities, the performance benchmark should be defined based on three main parameters: penetration depth, spatial and temporal resolutions [3, 5]. Spatial resolution describes the minimum imaging distance to distinguish two objects. Temporal resolution describes the minimum time to acquire the data for a single image. Penetration depth is the maximum distance of the imaging from the surface to the target object (usually defined as the distance where the signal intensity is reduced to $1/e$ [5]).

3.1.1 Magnetic

Magnetic field-based imaging allows for mapping of metallic materials, as well as anatomical structures due to spin of hydrogen atoms in soft tissue. There exist two main techniques for magnetic imaging – magnetic resonance imaging (MRI) (Fig. 3.1(a)) and magnetic particle imaging (MPI) (Fig. 3.1(b)).

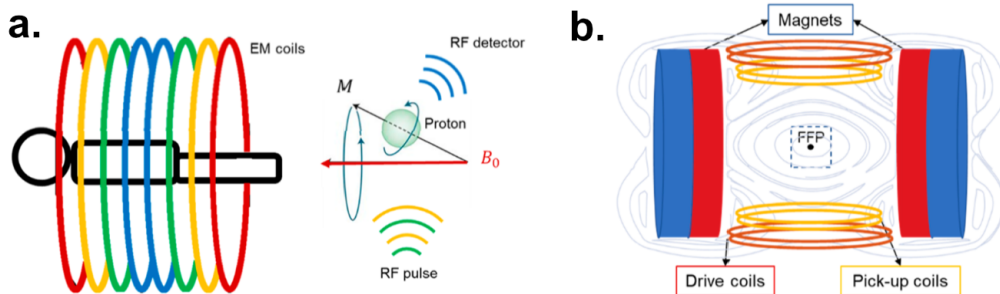


Figure 3.1: Magnetic imaging modality. **a.** MRI device produces strong magnetic field to align the protons in the body with that field. Radio frequency pulse (frequency of tens to hundreds of MHz) spin the protons out of equilibrium. The time it took to re-align and the amount of energy released depends on the material’s nature. **b.** MPI device uses drive coils to produce time-varying magnetic field, which saturates the tracers and induces voltage in receiver coils. The voltage corresponds to the concentration of magnetic particles and the location is found through field-free point produced by the permanent magnets. Adapted from [5].

MRI is widely used in clinical practice for 3D tissue imaging. It employs strong magnetic field and based on the atomic spin relaxation principle. Relaxation is the process by which a nuclear spin returns to a thermal equilibrium after absorbing radio frequency energy [4, 5]. The amount of released energy during re-alignment is measured and corresponds to the material nature. Originally, the technique is label-free, but magnetic materials can be employed to amplify the signal coming from micro-robots and improve SNR [4, 5]. However, this method produce imaging artifacts, which may reduce the localization accuracy [3]. MRI was mostly used to image swarms of micro-scale magnetic agents, while single agent imaging has only been demonstrated in millimeter scale [3–5, 21]. Spatial resolution can be increased by longer acquisition time. The temporal resolution of the MRI is low (in order of minutes), therefore the affordable trade-off between spatial and temporal resolution needs to be defined [5].

MPI allows to image the 3D distribution of magnetic particles, based on non-linear response of these particles to magnetic fields. MPI still requires more research and was only used for imaging milli-scale

magnetic helical swimmers and swarms of magnetic nano-scale particles [2, 5]. The spatial resolution for this technique is low (in millimeter scale), while the temporal is high.

3.1.2 Ultrasound

B-mode ultrasound utilizes a pulse ultrasound wave that propagates inside the body. The tissue generates unique echoes based on their reflective properties which are sensed and analysed to produce an image of the area [3–5]. It is the most available, safe and cost-efficient technique [21]. The main limitation of this technique is spatial resolution, which is limited by the wavelength of the pulse. Ideally, the axial resolution is half of the transmitted pulse, but scattering, diffraction and reconstruction process worsen it [4, 5]. In presented literature, to achieve higher spatial resolution, the frequency of the pulses is increased, reducing the penetration depth [5]. To improve the contrast of the agent, majority of works image micro-scale agents withing scarcely echogenic and still media [5] or detect micro-bubbles produced by agent’s movement [2–4]. The advantage of this technique is high penetration depth and imaging speed [2, 5]. The ultrasound imaging was performed on micro-scale magnetic single agents and swarms, milli-scale magnetic robots, millimeter-size swarm of nano-particles, etc. [3, 5, 21].

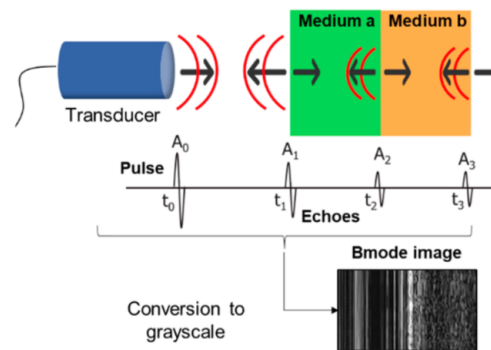


Figure 3.2: Ultrasound imaging modality. The emitted pulse interacts with the media and generates echoes, which are reconstructed into an image. Adapted from [5].

The alternative approach called ultrasound localization microscopy uses the signal scattered by the micro-bubbles by acquiring thousands of frames to resolve images below the acoustic diffraction limit. Such approach increases spatial but decreases temporal resolution and requires big amount of contrast material [5].

Doppler imaging is an ultrasound technique based on a Doppler effect, where the waves interact with a moving object, changing their frequency corresponding to the velocity of the object [2, 5]. The research is lacking on this imaging technique; it was only used for the detection of micro-scale agents and swarm of gas-filled nano-particles. Doppler imaging is better suited for detection of micro-robots in highly echogenic and dynamic environments [5].

3.1.3 Ionizing Radiation

The ionizing radiation imaging uses high-frequency radiation as a detection method. It has an advantage of high penetration depth but has an obvious downside of short use time to reduce radiation exposure [4, 5, 21]. There are two types of electromagnetic radiation used – X-rays and Gamma-rays. Fig. 3.3 depicts the working principle of all the techniques.

The computed tomography (CT) uses X-rays to ionize the atoms in the imaging path. The detector picks up the radiation and measures the difference in its absorption. The absorption depends on the material properties which is used to localize the micro-robots [2, 3, 5]. Bones and metallic agents produce higher contrast with respect to the tissue, while agents made from soft or polymeric materials need to be embedded with contrast-enhancing compounds [5]. Higher spatial resolution limits the CT’s temporal resolution due to the increased acquisition time. CT was scarcely researched for micro-robot imaging, except for several magnetic milli- and micro-robots [2, 5, 21]. Fluoroscopy is a two-dimensional (2D) X-ray-based imaging technique (visualizing the flow) working in real-time. Although it has higher temporal resolution and penetration than CT, the spatial resolution is lower [3, 5]. Fluoroscopy was not used for micro-robots imaging, only in procedures with needle/catheter steering.

The PET and SPECT rely on detection of Gamma-rays produced by radioactive tracers (radiotracers in short) attached to the micro-robots. The detector senses the Gamma-rays and localize the target using

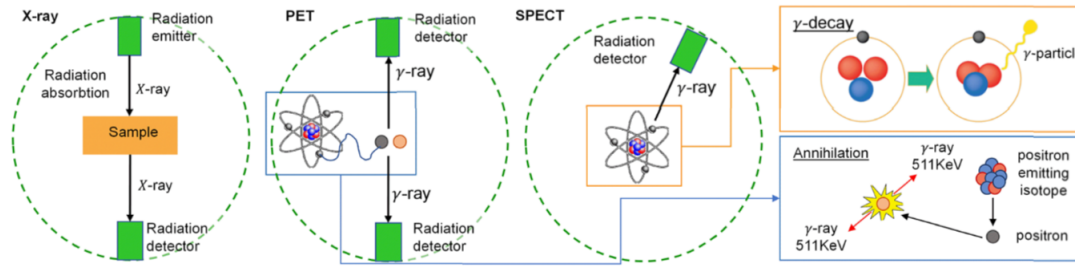


Figure 3.3: Ionizing radiation imaging modality. The X-ray method detects micro-robots due to difference in absorption of radiation. The positron emission tomography (PET) works by Gamma-ray detection due to positron-electron annihilation. The single photon emission computed tomography (SPECT) works by detecting Gamma-particles due to the decay. Adapted from [5].

3D reconstruction techniques [2, 5]. The techniques have a high penetration depth (tens of centimeters) but have low temporal resolution (from tens of seconds to more than a minute) and limited lifetime of radiotracers. Imaging was performed on a swarms of micro-motors and soft micro-robots as well as on a single milli-robot [5].

3.1.4 Optical

Initial optical imaging methods used bright field endomicroscopy with catheter-embedded camera and light source, providing robust tracking. Such catheters have limited access, low comfort and low spatial resolution [4]. Novel techniques utilize non-ionizing radiation and provide high spatial and temporal resolution, with main limitation of low penetration depth. To increase penetration, near-IR of 650-1350 nm is used for minimizing the absorption of the light by tissues. In addition, the depth is increased by embedding appropriate contrast agents in the micro-robots [5]. There are two techniques in optical imaging: fluorescence (Fig. 3.4(a)) and reflection (Fig. 3.4(b)) based [2, 5].

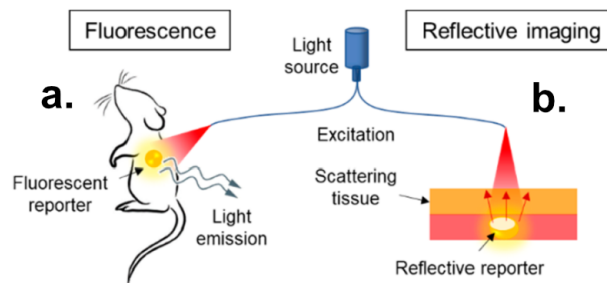


Figure 3.4: Optical imaging modality. **a.** Fluorescence imaging based on absorption and re-emission of light by the fluorophores. **b.** Reflective imaging based on intrinsic light-reflective properties of an object. Adapted from [5].

Reflection imaging relies on the intrinsic properties of micro-robots and tissues to reflect the light. Scattering of the tissue drastically reduces the SNR, thus penetration is hardly possible. To solve this issue, confocal microscopy is used, where out-of-focus light is filtered out using a pinhole [5]. The improved reflection-based technique called optical coherence tomography (OCT) improves spatial resolution and penetration but increases the acquisition time [2, 5]. OCT was used for imaging micro-/milli-robots and swarms of micro-agents [2, 5].

Fluorescence imaging is based on electron transition between energy states described in Chapter 2.1 (single photon excitation). In comparison to the previous method, the light is not being reflected but absorbed, so that a light of a different wavelength is emitted. The older works showed some level of penetration (several hundreds microns) but required long acquisition times (tens of seconds) and had quite low spatial resolution (larger than a hundred microns) [4, 5]. Recent research by Kaya et al. [22] show spatial resolution in order of microns and acquisition rate of 15 Hz, but no penetration depth. The imaging was performed on various single micro-robots and swarms of micro-agents [4, 5, 21, 22]. Because of the penetration depth, the better choice of using this technique is in exposed organs and tissues [5].

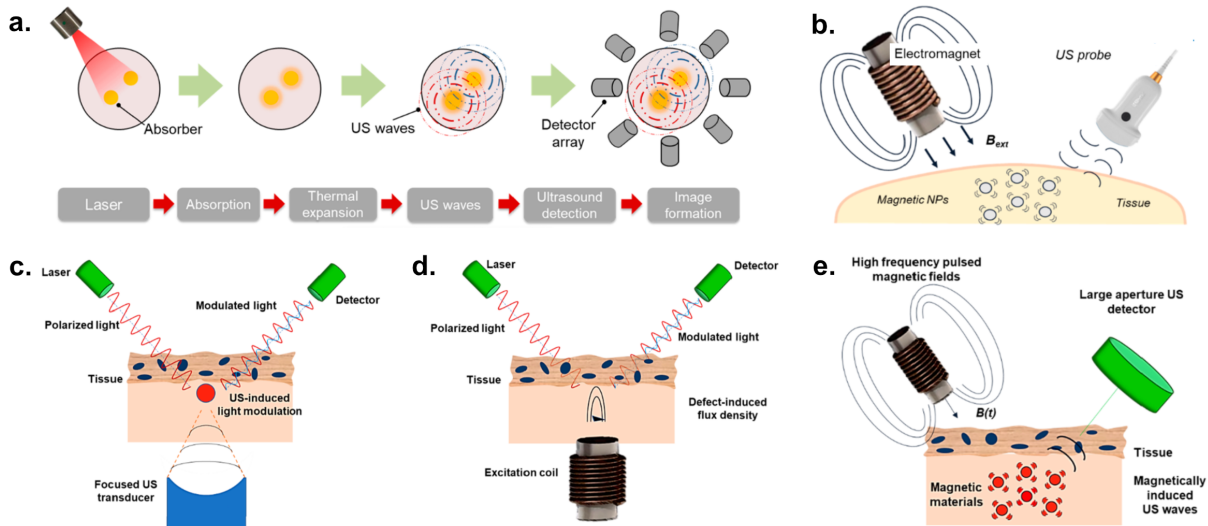


Figure 3.5: Multimodal imaging. **a.** PAI based on detection of light-induced thermal expansion and generation of pressure waves. **b.** MMUS based on detection of magnetic field-induced vibrations. **c.** Acousto-optic imaging based on ultrasound-induced light modulation. **d.** Magneto-optic imaging based on defect-induced light modulation. **e.** Magneto-acoustic imaging based on magnetic field-induced ultrasound waves. Adapted from [5].

3.1.5 Hybrid

Hybrid techniques integrate two or more imaging modalities to improve the performance of the original technique [2].

The technique called photo-acoustic imaging (PAI) (Fig. 3.5(a)) combines optical and ultrasound (B-mode-based) modalities. By shooting short-pulsed light at an object, it undergoes thermoplastic expansion. This expansion produces pressure waves picked up by an ultrasound detector. The waves differ depending on the material optical properties and the wavelength of the light. PAI enables high selectivity of internal structures (due to tissue's chromophores) and miniaturized robots (due to contrast agents). PAI was performed on magnetic micro-robots and drug-loaded micro-capsules [2, 5].

Another hybrid technique called magnetomotive ultrasound imaging (MMUS) (Fig. 3.5(b)) combines ultrasound (Doppler-based) and magnetic modalities. When the external time-varying magnetic fields are applied, the miniaturized robots experience vibrations. The exposed area is scanned with the ultrasound probe to capture this motion. The localization is done with phase-shift evaluation of the signal, identifying the shifts cause by the motion. MMUS can measure both magnetic material presence, as well as surrounding structures. The imaging was performed on the swarm of nano-particles. The disadvantage of the technique is that it cannot quantitatively estimate the distribution of these particles and has low (tens of seconds) temporal resolution. Although the resolution matches the ultrasound one, MMUS is able to detect even nano-scale motion [5].

Other multimodal techniques include PET/MRI, PAI/OCT ultrasound/PAI and PET/CT imaging systems, combining the benefits of both modalities [2]. Several techniques lack experimental confirmation but introduce possibly feasible futuristic concepts. Acousto-optic imaging (Fig. 3.5(c)) uses focused ultrasound waves modulate the reflected polarized light, providing information about the reflective material. Magneto-optic imaging (Fig. 3.5(d)) shoots polarized light at the sample, at the same time inducing eddy currents. The defects in the surface produce magnetic flux which modulate the reflected light. Magneto-acoustic (Fig. 3.5(e)) imaging induces vibrations of the magnetic material using high-frequency magnetic fields. A large aperture ultrasound detector reads the pressure coming from ultrasound waves generated by the magnetic material [5].

3.2 Multiphoton fluorescence imaging

In the current literature, there is no research done regarding the use of multiphoton excitation for micro-robots imaging. Therefore, the state of the art setups for the tissue imaging are discussed.

In terms of penetration depth, a setup was presented by Parra et al. [23], where *ex vivo* 2P imaging of cleared mouse organs (several cleaning steps with a solution of 1:2 benzyl alcohol to benzyl benzoate and methanol) was performed using 740 nm femtosecond laser. The authors produced high resolution images

(1024×1024 and 4096×4096 pixels) reaching up to 1.7 mm in small intestine, 2.2 mm in lungs, 850 μm in brain, 1.4 mm at testes and 1.1 mm at kidneys with a 0.5 to 2 mm field of view (FOV). The authors noted, that non-cleared organs provided much less detail, reducing the quality of the image dramatically. In that case imaging depth barely reached 100 μm . Streich et al. [24] used 1300 nm femtosecond laser for *in vivo* three-photon (3P) deep brain imaging, reaching a depth of 1.2 mm in cortex and 1.4 mm in hippocampus regions. *In vivo* brain imaging was also performed by Rodriguez et al. [25] through both 2P (920 nm) and 3P (1300 nm) excitation. With 2P imaging they achieved 513 μm penetration in mouse cortex; 767 and 952 μm penetration with 3P imaging in cortex and hippocampus. Unique approach was demonstrated by Kobat et al. [26], where 1280 nm laser was used for *in vivo* 2P excitation in mouse cortex. In order to image the cortical vasculature, the authors injected labeling liquid. The imaging depth of 1.6 mm was achieved with a frame rate of 1 Hz. The 300 μm^2 FOV was imaged at 512×512 pixels resolution.

High speed acquisition is another crucial parameter for real-time tracking. Veilleux et al. [27] showed the best performance, building a video rate *in vivo* 2P imaging setup. The 30 frames/s acquisition of high resolution (500×500 pixels) images of mouse skull bone marrow and ear dermis was achieved (FOV of 450 μm^2). The major downside of the setup is the penetration depth – 60 μm for bone marrow and 100 μm for ear dermis. Even at this depth, the selectivity was low relatively to the setups mentioned above. Yildirim et al. [28] presented *in vivo* 3P imaging of mouse cortex at 4 frames/s. Using 1300 nm femtosecond laser, a depth of 600 μm was reached. The authors stated that imaging a 250 μm^2 area with 256×272 resolution, the frame rates of up to 8 Hz are possible. A very remarkable work is shown by Ouzounov et al. [29] in which they achieved 2P and 3P imaging of intact mouse brain at 920 and 1300 nm excitation wavelength. Frame rates of up to 8.49 Hz for 200 μm^2 FOV of 256×256 resolution were reached. 2P excitation accomplished 780 μm depth, while 3P reached 1.1 mm.

Multiphoton imaging in humans is used in several *in vivo* studies. Breunig et al. [30] performed 2P skin imaging using 800 nm femtosecond laser. The layers at 20 and 30 μm depth were imaged. To produce 512×512 pixels image of 150 μm^2 area 7.4 s were required. Another study by Koenig et al. [15] showed deeper penetration of 320 μm under human skin.

The research towards miniaturization of the multiphoton setups focuses on reducing the size of scanner and objective in order to integrate them in a millimeter-size catheter. Ducourthial et al. [31] presented a fiber-optic endomicroscope enclosed into a probe with 2.2 mm outer diameter. Using a 810 nm femtosecond laser, they performed *ex vivo* 2P imaging of human tissues, reaching up to 300 μm depth. Similar penetration was achieved during *in vivo* imaging of a mouse kidney. The authors recorded *ex vivo* images with FOV of 250 μm^2 and *in vivo* with FOV of 450 μm^2 at 8 frames/s. More recent work by Park et al. [32] shows even higher frame rate of up to 26 Hz. The developed probe has 2.8 mm outer diameter and performs 2P imaging at 800 nm wavelength. With a FOV of 150 μm^2 , two types of images can be obtained – 1490×1024 pixels (circumferential × radial) at 3.3 frames/s or 1490×128 pixels at 26.6 frames/s. At 26.6 frames/s, the authors digitally reconstruct the pixels into 512×512 image. No penetration depth was stated in the paper.

Reviewing the presented literature on MPM of tissues, certain trends can be noticed. Firstly, the articles in which the deepest penetration of imaging was achieved, did not report adequate frame rate (mostly ≤ 1 frame/s). Accordingly, the works with higher temporal resolution either report smaller FOV or lower penetration depth. The applications with uncleared organs and *in vivo* show less penetration due to the presence of body liquids and dynamic environment. Most of the works used a frequency of ≈ 80 MHz Ti:Sapphire lasers with a pulse width no longer than 150 fs. All of the setups reported sub-cellular resolution.

3.3 Discussion

A schematic summarizing the state of art micro-robot imaging is presented at Fig. 3.6. In terms of the spatial and temporal resolutions, the multiphoton fluorescence imaging is the closest to the clinically-relevant zone among all of the other techniques.

Magnetic imaging does not provide enough spatial resolution. Moreover, as the magnetic actuation systems are prevalent for micro-robot control, interference between actuation and imaging systems may occur. The solution to this problem is typically the use of time-sharing, where the algorithm switches between the two magnetic systems, degrading the performance of both [2, 5]. Ultrasound is a robust imaging modality for real-time tracking of milli-/micro-robots but has a limited resolution. It cannot track the single micro-robots with the size of less than 100 μm . Ionizing imaging requires long acquisition times and has risks associated with the radiation exposure. Optical imaging has the downside of low penetration

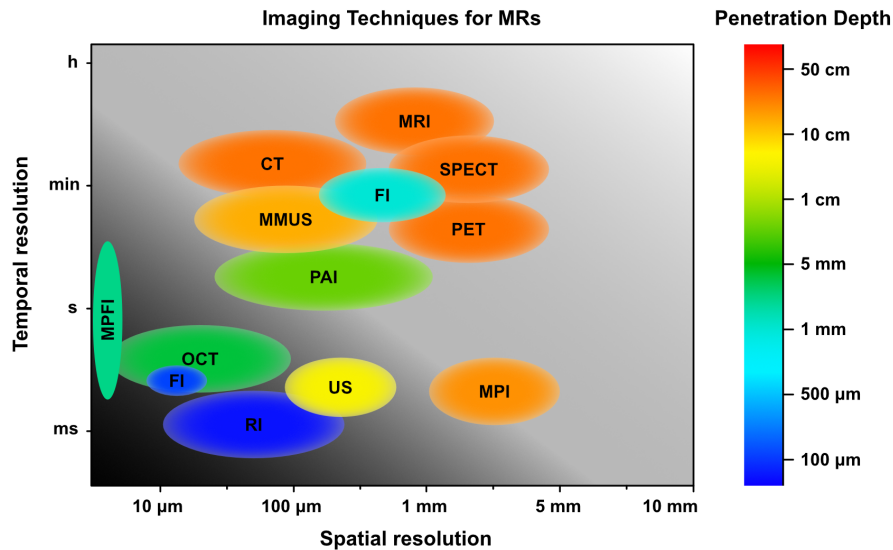


Figure 3.6: State of the art of medical micro-robots imaging. Spatial resolution, temporal resolution and tissue penetration depth overview of the medical micro-robots imaging techniques: MRI, MPI, ultrasound (US) imaging, CT, PET, SPECT, PAI, MMUS, reflection-based imaging (RI), fluorescence imaging (FI), OCT and multiphoton fluorescence imaging (MPFI). The darker the region, the better it is suited for clinically-relevant tracking of miniaturized agents. Adapted from [5].

depth. Hybrid techniques require more research to prove their relevance for clinical applications. Amongst hybrid methods PAI seems quite promising, having a good compromise among all of the three benchmark parameters – penetration, temporal and spatial resolutions.

Most methods with high penetration depth, either compromise with low spatial or low temporal resolutions. Therefore, fast and accurate imaging modalities would better fit for localized procedures with close contact with the target tissue. Although MPM provides relatively low penetration depth, it has a possibility of being miniaturized and used at deeply-seated regions of the human body (further discussed in Chapter 6.2).

Chapter 4. Multiphoton imaging setup

This chapter presents the setup used for 2P fluorescence imaging. The hardware is briefly discussed in section 4.1. Section 4.2 presents the software architecture of the setup and explains the acquisition and processing of the fluorescence image.

4.1 Hardware

Physical 2P setup use for micro-robot imaging is presented at Fig. 4.1 and was called multiphoton femto-imaging (MP-fi) setup. The whole setup is placed in a partially isolated chamber, to minimize the exposure to external light.

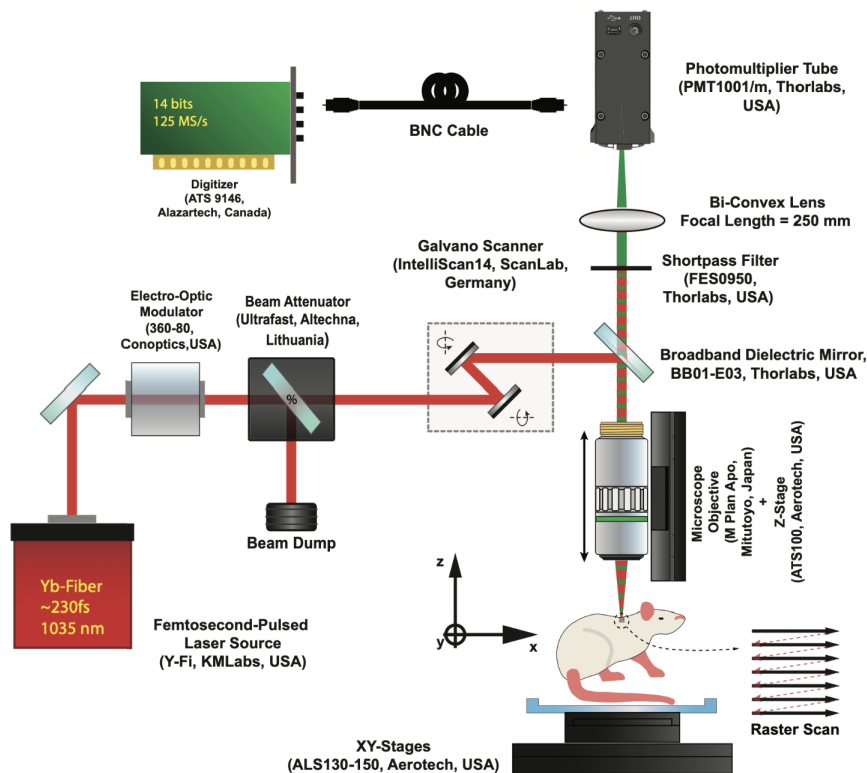


Figure 4.1: Schematic representing optical layout, acquisition, and scanning pattern of the MP-fi setup developed for imaging fluorescent microrobots inside the animal tissues. Made by dr. L. Capuano, Surgical Robotics Lab.

MP-fi setup is based on a femtosecond laser source with a pulse duration of ≈ 230 fs and a wavelength of $\lambda = 1035$ nm. The pulse repetition rate of the laser is controlled with electro-optic modulator. Maximum allowed frequency is 15 MHz. Energy of the pulse is changed by the beam attenuator.

A galvano-scanner with two rotating mirrors is used for stirring the laser beam across the specimen in XY plane. The galvo is controlled with real-time control (RTC) card designed for real-time control of scan heads via PC. The card is also connected to the trigger input of a data acquisition (DAQ) card to provide a synchronous acquisition of the signal.

The beam is focused on the sample with a microscope objective. The specimen can be moved with a XY-stage, while the objective with a Z-stage. The fluorescent light produced by 2P absorption passes through the microscope objective, a shortpass filter (which filters out any reflection from the original near-IR light) and a tube lens before being captured by a PMT. The output voltage produced by the PMT in response to the incoming fluorescent light corresponds to the local concentration of fluorophores. This analog signal is digitized using the DAQ card with a resolution of 14 bits and a maximum sample rate of 125 MS/s. The measured FOV in the XY-plane is $\approx 450 \mu\text{m}^2$ for the 10X lens ($\text{NA} = 0.28$) and $\approx 2000 \mu\text{m}^2$ for the 2X lens ($\text{NA} = 0.055$).

4.2 Software

4.2.1 General architecture

The software is coded in Python, it has an architecture where the high-level commands are processed into low-level ones and eventually communicate with the hardware. The program provides hardware communication with: (1) stages to move the specimen and objective in order to shift focus and scanning area, (2) RTC card for laser shutter (on/off command) and galvo control, as well as sending acquisition-start (trigger) signals to DAQ card, (3) DAQ card for the signal acquisition. The simplified software architecture diagram is presented on Fig. 4.2.

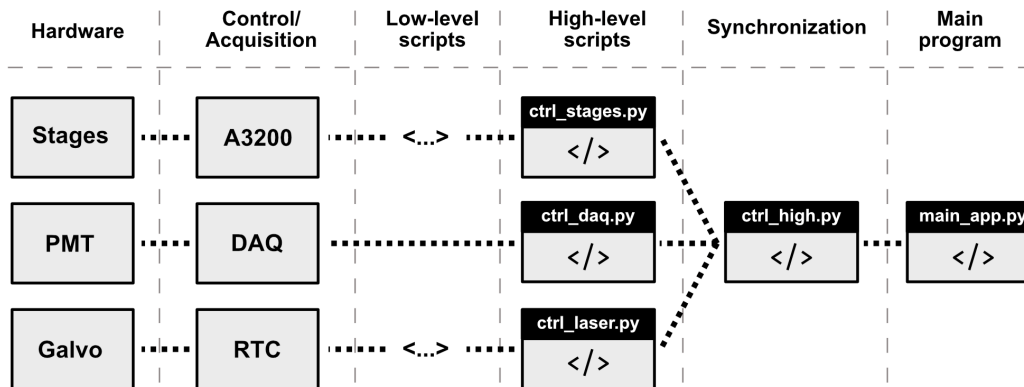


Figure 4.2: Software architecture of the MP-fi setup. Dashed line shows one/two way communication between nodes.

The core of the program is the `main_app.py` script, which calls the GUI. It is build with Qt5 widget toolkit. The script provides an interface between buttons/labels and high-level function calls. The `ctrl_high.py` script carries initialization and synchronization functionality. It contains high-level calls to lower-level scripts and ensures the software synchronization during scanning. The `ctrl_laser.py` provides communication with the RTC card, controlling the galvo steering of the beam. The `ctrl_daq.py` communicates with the DAQ card, performs the image acquisition and processing. The `ctrl_stages.py` communicates with XYZ-stages. The program uses the threading library which allows for concurrent execution of multiple functions. The structure is based on a worker-sender loop approach, where each of the high-level scrips has one or both loops running concurrently. Worker loop executes the calls from higher-level script/function while sender loop returns the data to it.

4.2.2 Image Acquisition

Image acquisition in MPM is based on a synchronous excitation and acquisition of the fluorescence signal. In order to produce a digital image, the voltage at PMT output is digitized while the laser beam moves across the image field. The scan is performed in a raster uni-directional pattern. The algorithm for the scanning pattern is shown in Appendix A.1.

The first step is to configure the DAQ. The main acquisition settings are: (1) capture clock (sampling rate and clock edge), (2) input channel (voltage range), (3) input trigger (threshold voltage). The PMT settings are adjusted real-time through the dedicated software.

Fig. 4.3 shows the hardware synchronization procedure. As the mirror of the galvo corresponding to the scanning in the X-direction moving, the trigger is sent to the DAQ indicating the start of the acquisition of the line. The DAQ card collects and transfers the data associated with the line to the PC memory as a 2-byte (16-bit) value. At the end of the line scan, the simultaneous rotation of X- and Y-axis mirrors produces diagonal movement, switching to the next line. The procedure repeats until all the lines are scanned, allowing the raw voltage data to be processed to produce a coherent image. After the image is built, the DAQ is again set to capture mode and the scanning commands are sent to the RTC, starting a new imaging cycle. The software is able to identify the troubles in data collection. As the number of lines to scan is known, the DAQ expects to receive the same amount of triggers. If it does not receive them in anticipated time – the imaging cycle resets.

The amount of data samples DAQ card collects per trigger ($S_{line} \in \mathbb{N}$) must correspond to the time galvo needs to scan the line ($t_{line} \in \mathbb{R}$), otherwise the synchronous acquisition cannot be achieved.

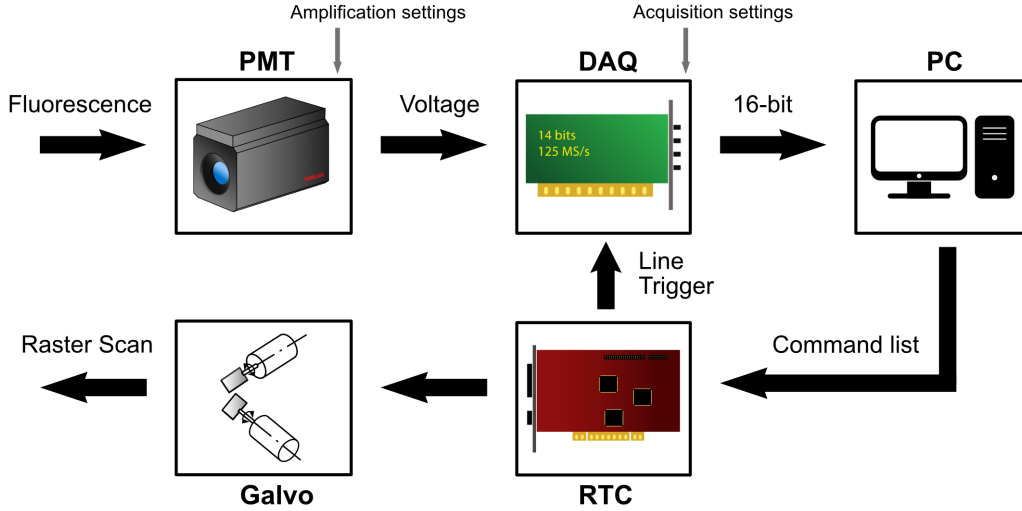


Figure 4.3: Schematic showing the hardware synchronization at the base of the acquisition of the fluorescent signal in the MP-fi setup.

Therefore, the S_{line} depends on two parameters – capture clock ($f_{capture} \in \mathbb{N}$) of the DAQ and t_{line} . The relation is shown at equation (4.1).

$$S_{line} = t_{line} \cdot f_{capture} \quad (4.1)$$

The DAQ card uses AlazarTech’s dual port memory technology. It can simultaneously record and transfer the data. While one of the board’s buffers is getting filled, the other is transferring data to PC memory. The card samples voltage across 0x0000 (hexadecimal number corresponding to negative full scale input) to 0xFFFF (hexadecimal number corresponding to positive full scale input).

The software synchronization is handled by the `ctrl_high.py` script, which ensures that the scanning starts when the DAQ card is in capture mode and ready to receive triggers from the RTC card. It also handles the interruption of the scanning with a stop button on the GUI. When this button is pushed, the laser’s shutter closes and the galvo stops. The software is then reset and ready for a new imaging cycle.

4.2.3 Image Processing

Image formation procedure is depicted at Fig. 4.4. The processing starts with the summation of the sampled data over the pixel dwell time (the time the laser beam stays on a single pixel). As expressed in equation (4.2), the amount of samples summed per pixel ($S_{pixel} \in \mathbb{N}$) is equal to the number of samples per line ($S_{line} \in \mathbb{N}$) divided by the number of lines, same as the number of pixels ($N_{pixels} \in \mathbb{N}$).

$$S_{pixel} = \frac{S_{line}}{N_{pixels}} \quad (4.2)$$

The conversion of the summed voltage ($V_i \in \mathbb{N}$) to a grayscale value ($G_i \in \mathbb{N}$) is achieved via equation (4.3), where $i \in \mathbb{N}$ represents the index of the value in the array. The voltage array is normalized across 16-bit (from 0 to 65535 in decimal representation).

$$G_i = 2^{16} \frac{V_i - V_{min}}{V_{max} - V_{min}} \quad (4.3)$$

The resultant image at this stage usually lacks brightness. To solve this issue, a dynamic brightness adjustment tool was introduced, expressed in equation (4.4). It works with the brightness factor $k \in \mathbb{R}$ which multiplies the original grayscale value $G_i \in \mathbb{N}$. The dynamic component is connected to the original value of the pixel, where the bright pixels are less amplified than the dark ones. To prevent a possible overflow, the values are truncated by the 16-bit limit.

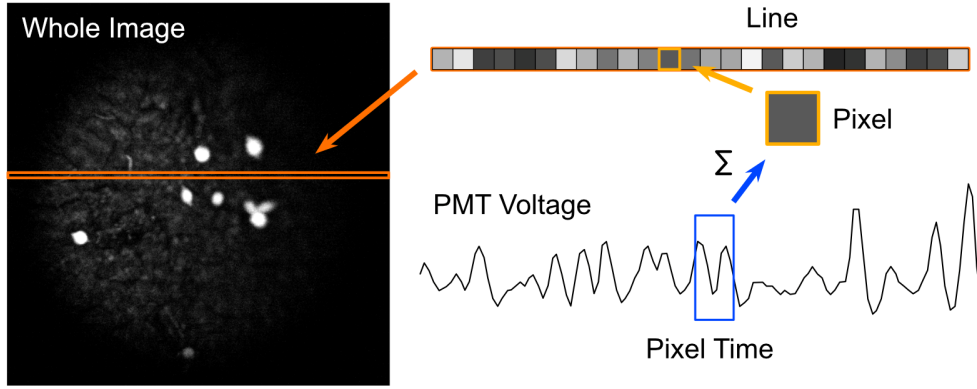


Figure 4.4: Image formation procedure. The grayscale value of each pixel is produced by binning (summing) the voltage array values across a defined bin size (pixel time). Adapted from [33].

$$G_{bright,i} = G_i \left(1 + k \frac{2^{16} - G_i}{2^{16}} \right) = \begin{cases} 0 & \text{if } G_{bright,i} < 0 \\ 2^{16} & \text{if } G_{bright,i} > 2^{16} \end{cases} \quad (4.4)$$

Image averaging functionality is added to improve the SNR. The difference in implementation is that an additional dimension is added to the voltage array, where the acquired data from several scans is stored. The mean value at each index (value position) across all the collected arrays is found. The averaged voltage array is then processed as usual. The resultant grayscale array is returned to `main.py` and assigned to the 2D image grid on the GUI.

4.2.4 Software Performance

The performance is mainly limited by the galvo scanning speed. Typical single frame acquisition times range between 3 and 4.7 seconds, depending on the scanning speed. The performance evaluation is presented in table 4.1. The raw processing time (time for image formation without use of brightness or averaging) is 140 ms at slowest. Dynamic brightness adjustment does not add any significant delay, while frame averaging function slows the computation time proportionally to the amount of acquired data. Additional performance tests were conducted, reducing the FOV ($\approx 100 \mu\text{m}^2$ for 10X, $\approx 500 \mu\text{m}^2$ for 2X objective) and scanning with $v = 200 \text{ mm/s}$, a framerate of 3 Hz was reached. The calculations in (4.3) and (4.4) are done using C language. External C script was generated, which allows to achieve a 4x speed improvement over computations directly in Python.

Table 4.1: Software performance evaluation for two different scanning velocities.

Scan speed v [mm/s]	Pixel dwell time [μs]	Acquisition time [s]	Processing time [ms]	Brightness tool time [ms]	5-frame averag- ing time [ms]
100	9.22	3	140	< 1	< 80
250	3.80	4.7	130	< 1	< 20

4.2.5 Software Interaction

The interaction with the software happens through a custom-built GUI, shown on Fig. 4.5. At first, user needs to initialize the hardware (Fig. 4.5 - ①). After successful initialization, sample and objective can be repositioned by moving the linear stages (Fig. 4.5 - ⑤). Next, the user can input the acquisition and processing parameters, as well as log data, if needed (Fig. 4.5 - ⑥). Pushing the set button (Fig. 4.5 - ⑦), the imaging parameters are configured. The laser beam power can then be tuned (Fig. 4.5 - ③). To start the imaging procedure, start button is pushed (Fig. 4.5 - ⑧). The stop button (Fig. 4.5 - ⑨) allows to abort the process and quit the imaging. Finally, the save button (Fig. 4.5 - ⑩) stores the image and associated DAQ output to the PC memory.

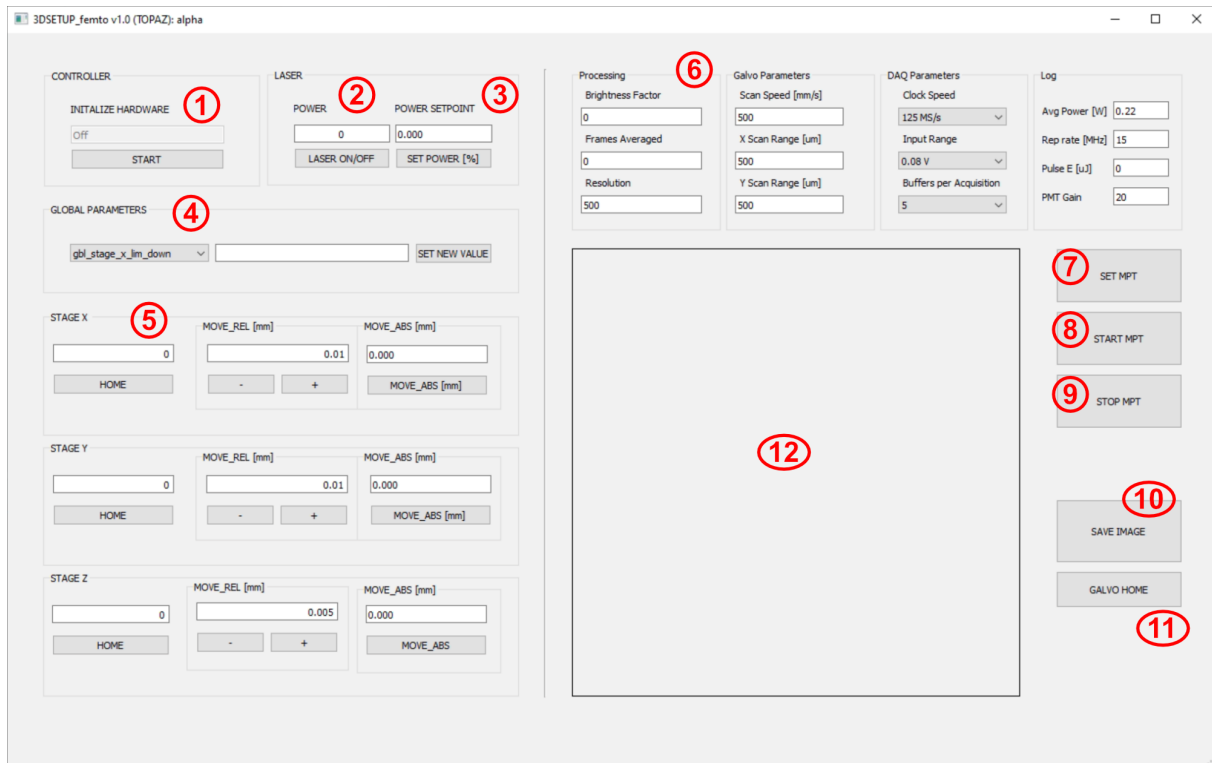


Figure 4.5: GUI of the MP-fi setup. Procedure to start the imaging: ① Initialize the hardware. ② Open/close the laser shutter. ③ Set the laser beam power. ④ Change global parameters (*e.g.* stages limits). ⑤ Position the stages. ⑥ Input the acquisition and processing parameters. ⑦ Set acquisition and processing parameters. ⑧ Begin imaging. ⑨ Stop imaging. ⑩ Save Log of the experiment. ⑪ Position the galvo mirrors to the home position. ⑫ Live visualization.

Chapter 5. Results and discussion

5.1 Materials and methods

The tissues used for the experiments in this study are taken *ex vivo* from common meat chicken and naive albino rats. The rats are sacrificed in the framework of another study according to the 3R (replacing, reducing and refining) principle which promotes the reuse of animal cadavers. From the chicken, only leg muscle and shaved skin are used; from the rats – leg muscle, brain and liver. The organs exported from the rats are extracted directly after sacrifice and used for experiments within 4 days, with storage at 4°C.

Experiments can be divided into two types: single-bot and swarm imaging. CeFlowBot (Fig. 5.1(a)) [34] used for single-bot imaging is 3D micro-printed with IP-Dip photoresin which has autofluorescence properties. The emission spectrum of such resin has a maximum centred at 478 nm, under a 405 nm excitation [35]. Another miniaturized agent used for the single-bot imaging is called micro-propeller (Fig. 5.1(b)) [36]. It is fabricated with the same IP-Dip photoresin. For the swarm imaging experiments, tiny micro-robots called flagella-bots (Fig. 5.1(c)) are employed. They are fabricated using coumarin-6 as a hydrophobic fluorophore allowing for 2P fluorescence imaging. Peak excitation and emission wavelengths for micro-agents are measured at 461 nm and 505 nm respectively. The size of these bots can vary with diameters down to 2-3 μm for the tails and 15-25 μm for the heads. Overall length of the flagella-bots can reach up to 200 μm .

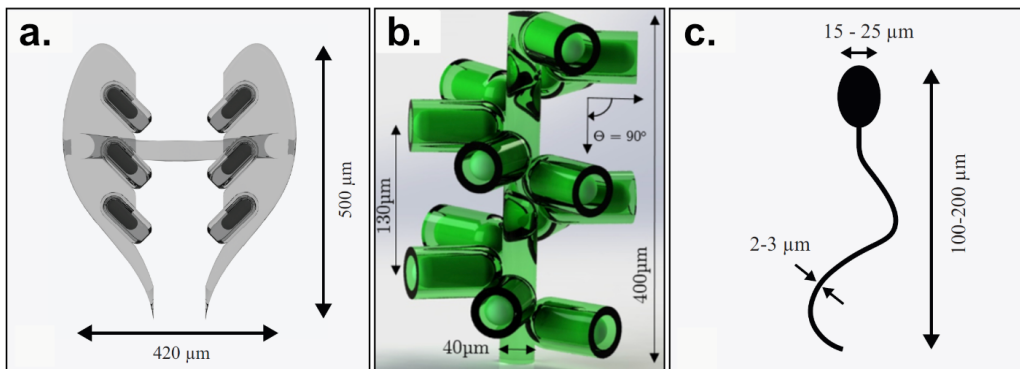


Figure 5.1: Schematics of the miniaturized agents. **a.** CeFlowBot. **b.** Micro-propeller. **c.** Flagella-bot.

Surface-level imaging is performed by placing the micro-robots on a water droplet. To perform the in-tissue experiments, first the micro-robots are placed on the surface of a borosilicate glass microscope slide. For the flagella-bots, a swarm of them mixed with DI-water is deposited with the help of a pipette. The CeFlowBots can be singularly deposited using a needle. After the deposition, a small portion of the organ is cut with a surgical scalpel and accurately placed above the micro-robots. A second glass slide is positioned on the tissue. This allows to flatten the surface and measure the thickness of the tissue. The thickness is measured by placing spacers between the slides of known width. The focus of the laser is then positioned through the top glass slide on the plane of interest.

All the experiments were performed in the laser laboratory of the Chair of Laser Processing of the University of Twente. The laboratory provides partial, but not perfect isolation from the external light sources.

5.2 Evaluation criteria

One of the major benefits of the multiphoton fluorescence imaging is its high resolution. According to the reviewed articles, a fundamental evaluation of the setup is how accurately it can image a micro-robot and whether it can reach sub-cellular ($\approx 1 \mu\text{m}$) resolution. Another criteria is the amount of information that can be derived from the image: position of the micro-robot, its orientation, surrounding structures, and how applicable it is for the tracking.

5.3 Single-bot imaging

The first experiments were made without tissue, imaging the micro-robots on a water droplet with the 10X objective. Obtained image of CeFlowBot is presented at Fig. 5.2(a),(b) and micro-propeller at Fig. 5.2(c),(d).

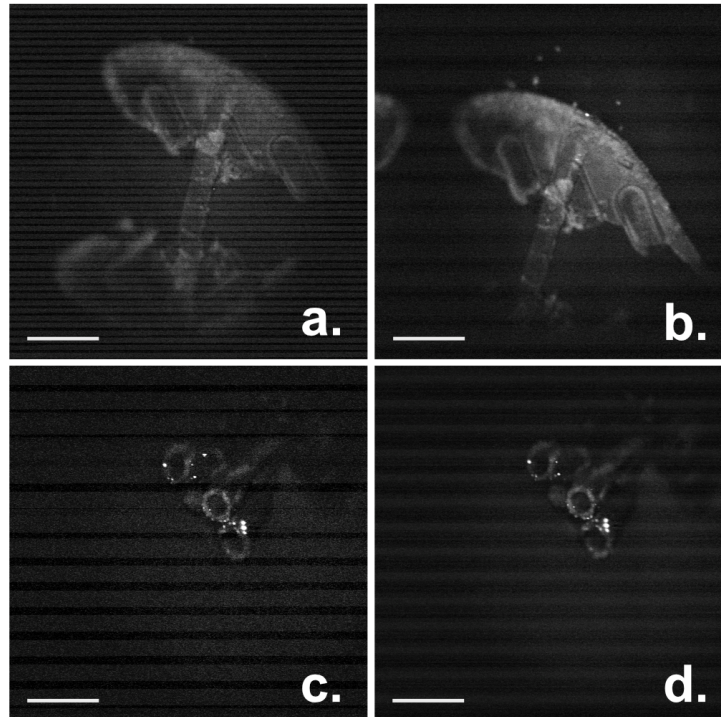


Figure 5.2: MPM of a CeFlowBot and micro-propeller on a water droplet. **a.** Single-frame acquisition of the CeFlowBot. Imaging was done with the following parameters: galvo linear velocity $v = 50$ mm/s, DAQ clock $f_{capture} = 50$ MHz, brightness factor $k = 3$ and resolution of 500×500 . **b.** Five-frame averaging of the CeFlowBot; parameters: same, except $v = 200$ mm/s. **c.** Single-frame acquisition of the micro-propeller; parameters: $v = 250$ mm/s, $f_{capture} = 50$ MHz, $k = 3$, resolution of 500×500 . **d.** Five-frame averaging of the micro-propeller; parameters: same. Scale bar = $100 \mu\text{m}$.

Further experiments include in-tissue imaging. CeFlowBot was placed below $\approx 100 \mu\text{m}$ of chicken skin. The result of the imaging with a 10X objective is shown on Fig. 5.3(a). During another experiment, the CeFlowBot was placed under rat muscle tissue with a thickness of $750 \mu\text{m}$ and imaged with a 2X objective. Result is shown on Fig. 5.3(b). Fig. 5.3(c) presents a magnified area where the CeFlowBot is overlaid with the original sketch.

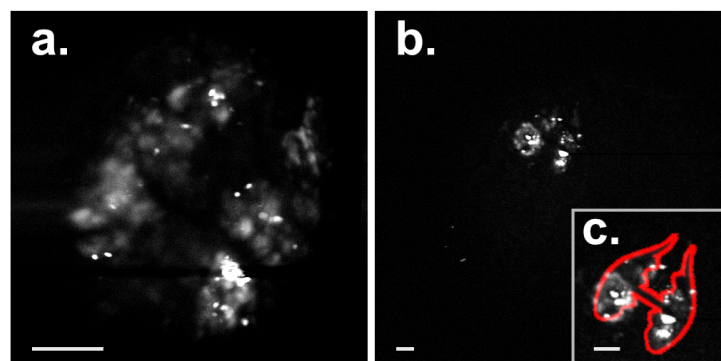


Figure 5.3: MPM of CeFlowBot inside tissue. **a.** The micro-robot inside $\approx 100 \mu\text{m}$ deep chicken skin; imaged with a 10X objective; parameters: $v = 200$ mm/s, $f_{capture} = 50$ MHz, $k = 3$, 500×500 resolution. **b.** 5-frame average of the micro-robot under $750 \mu\text{m}$ thick rat muscle tissue, imaged with a 2X objective; parameters: $v = 100$ mm/s, $f_{capture} = 50$ MHz, $k = 7$, 500×500 resolution. **c.** Magnified area with the CeFlowBot; the overlaid contour indicates the original shape of the bot. Scale bar = $100 \mu\text{m}$.

5.4 Swarm imaging

Surface-level experiments were initially performed as a test of swarm imaging. Fig. 5.4(a) shows the results of imaging with a 10X objective in a liquid solution. Fig. 5.4(b) depicts the flagella-bots on the surface of the rat's liver.

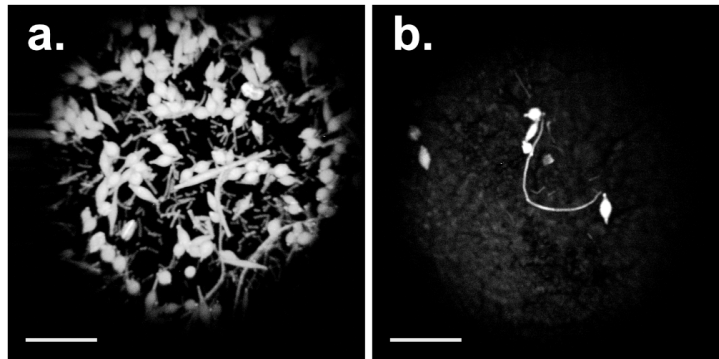


Figure 5.4: MPM of flagella-bots. **a.** Single-frame imaging in a liquid solution; parameters: $v = 100$ mm/s, $f_{capture} = 50$ MHz, $k = 1$, 500×500 resolution. **b.** Single-frame imaging on the surface of rat's liver; parameters: same, except the $v = 50$ mm/s and $k = 2$. Scale bar = $100 \mu\text{m}$.

Successful in-tissue imaging of the flagella-bots with a 10X objective is shown on Fig. 5.5(a), where the $200 \mu\text{m}$ brain tissue penetration was achieved. Results of an experiment with the injection of flagella-bots inside chicken skin tissue are presented on Fig. 5.5(b),(c). The MPM with a 2X objective was performed – first image (Fig. 5.5(b)) is done close to the surface, second (Fig. 5.5(c)), by moving $\approx 800 \mu\text{m}$ deep.

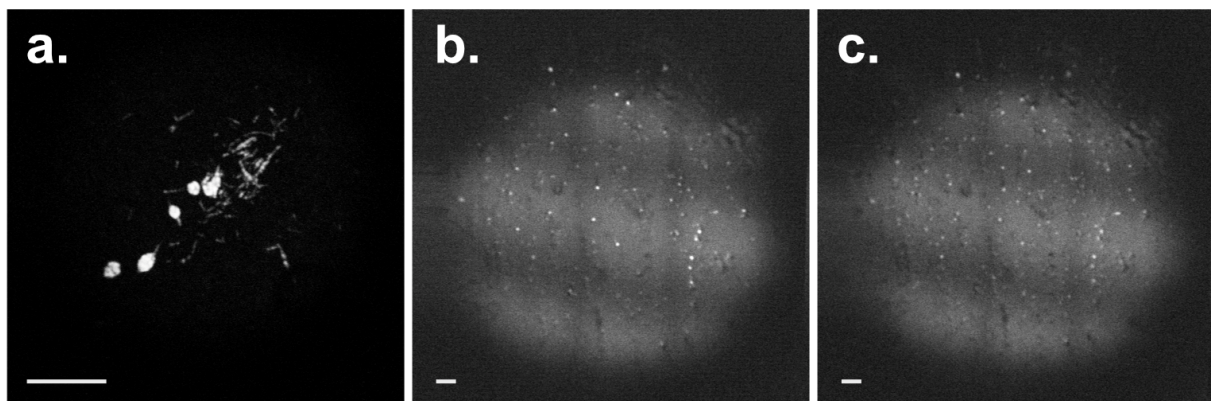


Figure 5.5: MPM of the flagella-bots. **a.** Flagella-bots imaged with a 10X objective under $200 \mu\text{m}$ of brain tissue; parameters: $v = 100$ mm/s, $f_{capture} = 50$ MHz, $k = 1$, resolution of 500×500 . **b.** 5-frame average of flagella-bots imaged with a 2X objective close to surface of the chicken skin; parameters: $v = 100$ mm/s, $f_{capture} = 50$ MHz, $k = 2$, resolution of 500×500 . **c.** Same experiment with flagella-bots imaging with a 2X objective $\approx 800 \mu\text{m}$ deep inside chicken skin. Scale bar = $100 \mu\text{m}$.

5.5 Discussion

Experimental results provided the images with an extremely high spatial resolution. The images of TPEF at Fig. 5.2 show high similarity to the original sketches of the robots. In swarm imaging, even using 2X lens with a $2000 \mu\text{m}^2$ FOV, individual flagella-bots can be distinguished. Moreover, imaging experiments at the surface with the 10X objective clearly show the tails of flagella-bots, demonstrating an accuracy of $\approx 1 \mu\text{m}$.

CeFlowBot showed promising results for in-tissue imaging. In Fig. 5.3, the black curved lines above the robot possibly present structures like capillaries emitting much lower fluorescence which makes a big contrast with the robot. Despite the bot being covered, as shown in Fig. 5.3(b),(c), certain information can be derived, including an approximate location, as well as the orientation of the bot.

Upon a close examination, some level of distortion can be observed close to the edges of the images, outside of the region of interest. According to the literature [33, 37], one of the most efficient methods for distortion correction in galvanometric-based laser scanning is increased scanning range (beyond the region of interest). That way, most of the distortions associated with such systems can be cropped out at later stages. In our case, the scan region spans beyond the lens, leading to minimal distortions in the region with the micro-robots.

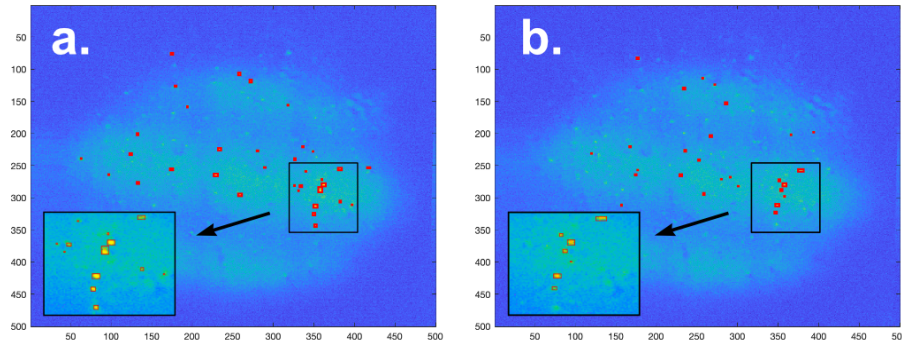


Figure 5.6: Detection algorithm of flagella-bots on in-tissue MPM images. Magnified area shows the cross-detection of bots at different depths. **a.** Bots detected close to surface of the chicken skin. **b.** Bots detected at $\approx 800 \mu\text{m}$ deep inside chicken skin.

Images presented at Fig. 5.5(b),(c) show that the flagella-bots are cross-detected at different penetration levels, i.e. even if the objective is shifted and the image plane is changed, the same micro-robots are detected by the system. It aligns with the theory presented in section 2.2, where lower NA (the 2X objective has a lower NA than the 10X one) objective increasing the absorption volume (focal spot), causing the detection of the agents from adjusted layers. Fig. 5.6 presents a simple algorithm written in MATLAB for the micro-robots detection. The grayscale image is converted to binary, where pixel has a value of 0 if below defined threshold, and 1 if above. Then, the program marks the regions of connected pixels above the threshold with a rectangle. Although there is a difference in the flagella-bots detection at different depths, both, Fig. 5.6(a) and Fig. 5.6(b) have cross-detected the same bots, especially in the magnified area. Bottom line here is that XY-axis tracking can still be relevant at such depth, while the Z-axis tracking is poor for an objective with low NA of 0.055.

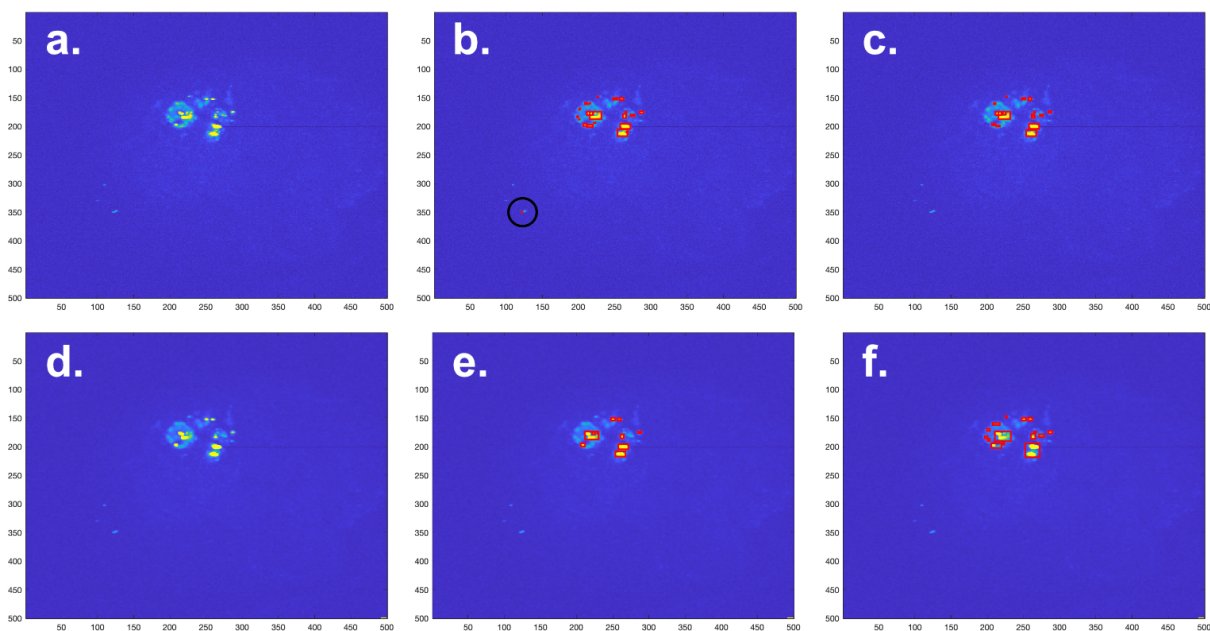


Figure 5.7: CeFlowBot imaged under $750 \mu\text{m}$ of rat muscle tissue. **a.** 5-frame average (5-FA). **b.** Detection algorithm applied at 5-FA. Black circle indicates noise (impostor pixels) being detected as the bot (genuine pixels). **c.** Detection algorithm with adjusted threshold applied at 5-FA – only genuine pixels are marked as the bot. **d.** 5-frame spatiotemporal rank filter (5-FSTR) of rank 0.8 applied to the original data. **e.** Detection algorithm applied at 5-FSTR. **f.** Detection algorithm with adjusted threshold applied at 5-FSTR.

5.6 Frame averaging

Experimental results show that image averaging increases the overall quality of the image, especially helping in removing the noise coming from the 50 Hz background illumination. However, as can be seen from the Fig. 5.7(b), the averaging does not remove the noise completely. Unknown noise signal is detected as part of the micro-robot by the binarization algorithm presented in the previous subsection. It can be easily avoided by simple adjusting the threshold, but in that case some of the information from the bot itself is removed (see Fig. 5.7(c)). In numbers, in Fig. 5.7(b) 498 pixels are detected as a part of CeFlowBot, while 425 in Fig. 5.7(c).

In this context, Pinkard et al. [38] presented a filter aimed at increasing the SNR of MPM images (Fig. 5.8). The authors developed a spatiotemporal rank filter, which, comparing to a standard averaging, also takes spatial component into account. Rank filter is based on a sliding window taking a set of values as an input (according to a window size), that sorts them in ascending order and sets a value of a center pixel according to the rank (from 0 to 1). A rank of 0.5 represents a median filter. Rank filter effectively eliminates impulsive noise but not the high spatial frequencies, preserving the details principal for an automated object detection [38]. Appropriate rank depends on the particular imaging environment. For their research, Pinkard et al. found the 0.8 rank lead to the best performance. Lower rank (*e.g.* medial filter) resulted in attenuation of weak signals, while higher rank failed to eliminate the background noise.

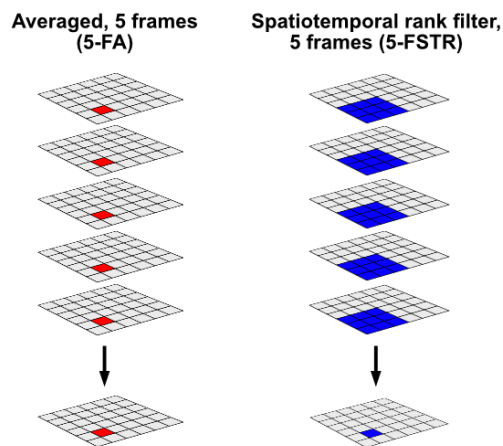


Figure 5.8: Comparison of conventional frame averaging (5-FA) to a spatiotemporal rank filter (5-FSTR). The 5-FSTR encodes both temporal and spatial information to produce a pixel. Adapted from [38].

Applying the spatiotemporal rank filter (rank = 0.8) to the data from Fig. 5.7(a) resulted in Fig. 5.7(d). Using the same threshold as in Fig. 5.7(b), the number of genuine pixels is 461, which is lower than with standard averaging. Nonetheless, as shown on Fig. 5.7(e), the noise pixels was correctly detected as impostor. Adjusting the threshold, the amount of pixels was increased to 814 (Fig. 5.7(f)). The bottom line here is that the spatiotemporal rank filter resulted in the detection of 1.9x more pixels belonging to the CeFlowBot, indicating better performance than the frame averaging.

Chapter 6. Conclusions

6.1 Achieved goals

The MP-fi setup presented in this work is able to image micro-robots inside tissues through the multiphoton fluorescence imaging. The experimental evidence prove that the setup can operate for different tissues at a depth of at least 750 μm for a single-bot imaging and 250 μm for a swarm imaging. Currently, the real-time monitoring cannot be achieved due to the galvo scanning speed. To make a high-quality 500 \times 500 pixels image, the speed between 100 and 250 mm/s is used. Imaging at a close-to-surface depth ($< 500 \mu\text{m}$), the higher speed of 250-500 mm/s may still provide enough information to locate the target. The current framerate with increased speed and reduced FOV can reach up to 3 Hz. Further experiments are required to evaluate the quality of the images at a higher scanning rates, as well as the maximum penetration depth of the setup, especially for the swarm imaging. The MP-fi software provides relatively fast image processing ($< 200 \text{ ms}$) and includes custom GUI that allows for control over imaging parameters and can efficiently log the experiments.

The MP-fi is a prototype setup built to prove the possibility to image the micro-robots inside tissues using multiphoton excitation process. It is a first step in using this technique for miniaturized agent tracking and further work must be done to make it suitable for a clinically-relevant use.

6.2 Future work

6.2.1 Hardware

Some of the limitations of the current setup can be solved by using equipment with higher or different specifications. Most of the research in the field of multiphoton fluorescence imaging was based on a higher-frequency ($\approx 80 \text{ MHz}$) femtosecond lasers. Such light source will be able to deliver the same amount of pulses in a shorter time, which will allow for a higher scanning speed. At the same time, higher wavelength light is able to penetrate deeper into tissues and can be used with highly red-shifted fluorophores for 2P excitation or more common ones for 3P excitation.

Further improvements can be achieved by using a more recent galvo/galvo-resonant scanner, allowing for more precise and seamless control over the laser steering and hardware synchronization through a proper low-level access to the device. Moreover, by reducing the scanning area while using the lower magnification objective, the FOV remains the same. Taking resolution into account, similar quality image can be obtained while the acquisition time is reduced (as the scan area is reduced).

The next step for the multiphoton imaging set-up must include miniaturization via use of fiber optics and microelectromechanical systems [31, 32]. A part of the setup can be put into a millimeter scale probe allowing the use of such endomicroscope for localized minimally invasive procedures at deeply-seated regions of the human body. Multimodal integration for a hybrid imaging can increase the penetration depth of the setup. For example, a promising technique like PAI, that requires light excitation, can supplement the multiphoton fluorescence imaging by sensing the ultrasonic waves emitted from the micro-robot due to its thermal expansion.

6.2.2 Software

Software improvement should focus on increasing the speed of computations which are still relatively slow for a real-time tracking. This processing can be transferred to a high performance device such as field-programmable gate array or to a graphics processing unit.

The fluorescence lifetime imaging (FLIM) is one of the fluorescence imaging techniques based on measuring the time duration of a fluorophore being in excited state before emitting a photon. This technique can be integrated with the current method for improved SNR and ability to distinguish the fluorescence source [39].

Bibliography

- [1] B. J. Nelson, I. K. Kaliakatsos, and J. J. Abbott, “Microrobots for minimally invasive medicine,” *Annual Review of Biomedical Engineering*, vol. 12, pp. 55–85, Aug. 2010, ISSN: 15239829. DOI: 10.1146/annurev-bioeng-010510-103409.
- [2] Z. Li, C. Li, L. Dong, and J. Zhao, “A review of microrobot’s system: Towards system integration for autonomous actuation in vivo,” *Micromachines*, vol. 12, 10 Oct. 2021, ISSN: 2072666X. DOI: 10.3390/mi12101249.
- [3] H. Ceylan, I. C. Yasa, U. Kilic, W. Hu, and M. Sitti, “Translational prospects of untethered medical microrobots,” *Progress in Biomedical Engineering*, vol. 1, 1 Jul. 2019, ISSN: 25161091. DOI: 10.1088/2516-1091/ab22d5.
- [4] F. Soto, J. Wang, R. Ahmed, and U. Demirci, “Medical micro/nanorobots in precision medicine,” *Advanced Science*, vol. 7, 21 Nov. 2020, ISSN: 21983844. DOI: 10.1002/advsc.202002203.
- [5] A. Aziz *et al.*, “Medical imaging of microrobots: Toward in vivo applications,” *ACS Nano*, vol. 14, pp. 10865–10893, 9 Sep. 2020, ISSN: 1936086X. DOI: 10.1021/acsnano.0c05530.
- [6] A. Ustione and D. W. Piston, “A simple introduction to multiphoton microscopy,” *Journal of Microscopy*, vol. 243, pp. 221–226, 3 Sep. 2011, ISSN: 00222720. DOI: 10.1111/j.1365-2818.2011.03532.x.
- [7] A. E. Bongo, “3d image processing of two-photon microscopy images depicting nanoprobe in skin,” Northeastern University, 2011.
- [8] F. He *et al.*, “Femtosecond laser fabrication of monolithically integrated microfluidic sensors in glass,” *Sensors*, vol. 14, pp. 19402–19440, 10 Oct. 2014, ISSN: 14248220. DOI: 10.3390/s141019402.
- [9] Y. Dancik, A. Favre, C. J. Loy, A. V. Zvyagin, and M. S. Roberts, “Use of multiphoton tomography and fluorescence lifetime imaging to investigate skin pigmentation in vivo,” *Journal of Biomedical Optics*, vol. 18, p. 026022, 2 Feb. 2013, ISSN: 1083-3668. DOI: 10.1117/1.jbo.18.2.026022.
- [10] D. W. Piston, T. J. Fellers, and M. W. Davidson, *Fundamentals and applications in multiphoton excitation microscopy*. [Online]. Available: <https://www.microscopyu.com/techniques/multiphoton/multiphoton-microscopy>.
- [11] K. König, “Clinical multiphoton tomography,” *Journal of Biophotonics*, vol. 1, pp. 13–23, 1 2008, ISSN: 1864063X. DOI: 10.1002/jbio.200710022.
- [12] W. R. Zipfel, R. M. Williams, R. Christie, A. Y. Nikitin, B. T. Hyman, and W. W. Webb, “Live tissue intrinsic emission microscopy using multiphoton-excited native fluorescence and second harmonic generation,” *PNAS June*, vol. 10, pp. 7075–7080, 2003. DOI: 10.1073/pnas.0832308100.
- [13] R. Paschotta, *Fluorescence microscopy*, 2021. [Online]. Available: https://www.rp-photonics.com/fluorescence_microscopy.html.
- [14] E. E. Hoover and J. A. Squier, “Advances in multiphoton microscopy technology,” *Nature Photonics*, vol. 7, pp. 93–101, 2 2013, ISSN: 1749-4893. DOI: 10.1038/nphoton.2012.361.
- [15] K. Koenig, “Hybrid multiphoton multimodal tomography of in vivo human skin,” *IntraVital*, vol. 1, pp. 11–26, 1 Jul. 2012, ISSN: 2165-9087. DOI: 10.4161/intv.21938.
- [16] P. Xi, Y. Liu, and Q. Ren, “Scanning and image reconstruction techniques in confocal laser scanning microscopy,” *Laser Scanning, Theory and Applications*, Apr. 2011. DOI: 10.5772/14545.
- [17] J. Huang, Q. Qin, J. Wang, and H. Fang, “Two dimensional laser galvanometer scanning technology for additive manufacturing,” *International Journal of Materials, Mechanics and Manufacturing*, vol. 6, pp. 332–336, 5 Oct. 2018, ISSN: 17938198. DOI: 10.18178/ijmmm.2018.6.5.402.
- [18] J. C. Waters, “Accuracy and precision in quantitative fluorescence microscopy,” *Journal of Cell Biology*, vol. 185, pp. 1135–1148, 7 Jun. 2009, ISSN: 00219525. DOI: 10.1083/jcb.200903097.
- [19] *Second harmonic generation*. [Online]. Available: <https://svi.nl/SecondHarmonicGeneration>.

- [20] A. C. Croce and G. Bottiroli, "Autofluorescence spectroscopy and imaging: A tool for biomedical research and diagnosis," *European Journal of Histochemistry*, vol. 58, pp. 320–337, 4 Dec. 2014, ISSN: 20388306. DOI: 10.4081/ejh.2014.2461.
- [21] J. Zhang, "Evolving from laboratory toys towards life-savers: Small-scale magnetic robotic systems with medical imaging modalities," *Micromachines*, vol. 12, 11 Nov. 2021, ISSN: 2072666X. DOI: 10.3390/mi12111310.
- [22] M. Kaya, F. Stein, J. Rouwkema, I. S. Khalil, and S. Misra, "Serial imaging of micro-agents and cancer cell spheroids in a microfluidic channel using multicolor fluorescence microscopy," *PLoS ONE*, vol. 16, 6 June Jun. 2021, ISSN: 19326203. DOI: 10.1371/journal.pone.0253222.
- [23] S. G. Parra, T. H. Chia, J. P. Zinter, and M. J. Levene, "Multiphoton microscopy of cleared mouse organs," *Journal of Biomedical Optics*, vol. 15, p. 036 017, 3 May 2010, ISSN: 1083-3668. DOI: 10.1117/1.3454391.
- [24] L. Streich *et al.*, "High-resolution structural and functional deep brain imaging using adaptive optics three-photon microscopy," *Nature Methods*, vol. 18, pp. 1253–1258, 10 Oct. 2021, ISSN: 15487105. DOI: 10.1038/s41592-021-01257-6.
- [25] C. Rodríguez *et al.*, "An adaptive optics module for deep tissue multiphoton imaging in vivo," *Nature Methods*, vol. 18, pp. 1259–1264, 10 Oct. 2021, ISSN: 15487105. DOI: 10.1038/s41592-021-01279-0.
- [26] D. Kobat, N. G. Horton, and C. Xu, "In vivo two-photon microscopy to 1.6-mm depth in mouse cortex," *Journal of Biomedical Optics*, vol. 16, p. 106 014, 10 2011, ISSN: 10833668. DOI: 10.1117/1.3646209.
- [27] I. Veilleux, J. A. Spencer, D. P. Biss, D. Côté, and C. P. Lin, "In vivo cell tracking with video rate multimodality laser scanning microscopy," *IEEE Journal of Selected Topics in Quantum Electronics*, vol. 14, 1 2008. DOI: 10.1109/.JSTQE.2008.912751.
- [28] M. Yildirim, H. Sugihara, P. T. So, and M. Sur, "Functional imaging of visual cortical layers and subplate in awake mice with optimized three-photon microscopy," *Nature Communications*, vol. 10, 1 Dec. 2019, ISSN: 20411723. DOI: 10.1038/s41467-018-08179-6.
- [29] D. G. Ouzounov *et al.*, "In vivo three-photon imaging of activity of gcamp6-labeled neurons deep in intact mouse brain," *Nature Methods*, vol. 14, pp. 388–390, 4 2017, ISSN: 15487105. DOI: 10.1038/nmeth.4183.
- [30] H. G. Breunig *et al.*, "Clinical coherent anti-stokes raman scattering and multiphoton tomography of human skin with a femtosecond laser and photonic crystal fiber," *Laser Physics Letters*, vol. 10, 2 Feb. 2013, ISSN: 16122011. DOI: 10.1088/1612-2011/10/2/025604.
- [31] G. Ducourthial *et al.*, "Development of a real-time flexible multiphoton microendoscope for label-free imaging in a live animal," *Scientific Reports*, vol. 5, Dec. 2015, ISSN: 20452322. DOI: 10.1038/srep18303.
- [32] H.-C. Park *et al.*, "High-speed fiber-optic scanning nonlinear endomicroscopy for imaging neuron dynamics in vivo," *Optics Letters*, vol. 45, p. 3605, 13 Jul. 2020, ISSN: 0146-9592. DOI: 10.1364/ol.396023.
- [33] T. A. Pologruto, B. L. Sabatini, and K. Svoboda, "Scanimage: Flexible software for operating laser scanning microscopes," *BioMedical Engineering OnLine*, vol. 2, 13 2003.
- [34] S. Mohanty, A. Paul, P. M. Matos, J. Zhang, J. Sikorski, and S. Misra, "Ceflowbot: A biomimetic flow-driven microrobot that navigates under magneto-acoustic fields," *Small*, 2021, ISSN: 16136829. DOI: 10.1002/smll.202105829.
- [35] A. Accardo *et al.*, "Multiphoton direct laser writing and 3d imaging of polymeric freestanding architectures for cell colonization," *Small*, vol. 13, 27 Jul. 2017, ISSN: 16136829. DOI: 10.1002/smll.201700621.
- [36] S. Mohanty *et al.*, "Acoustically-actuated bubble-powered rotational micro-propellers," *Sensors and Actuators B: Chemical*, vol. 347, Nov. 2021, ISSN: 09254005. DOI: 10.1016/j.snb.2021.130589.
- [37] W. Wang, Z. Wu, and H. Zeng, "Image distortion and its correction in linear galvanometric mirrors-based laser-scanning microscopy," *Journal of Biomedical Optics*, vol. 20, p. 056 001, 5 May 2015, ISSN: 1083-3668. DOI: 10.1117/1.jbo.20.5.056001.

- [38] H. Pinkard, K. Corbin, and M. F. Krummel, “Spatiotemporal rank filtering improves image quality compared to frame averaging in 2-photon laser scanning microscopy,” *PLoS ONE*, vol. 11, 3 Mar. 2016, ISSN: 19326203. DOI: 10.1371/journal.pone.0150430.
- [39] J. D. Driscoll *et al.*, “Photon counting, censor corrections, and lifetime imaging for improved detection in two-photon microscopy,” *Journal of Neurophysiology*, vol. 105, pp. 3106–3113, 2011. DOI: 10.1152/jn.00649.2010.

Appendix A. Additional material

A.1 Steering algorithm

The algorithm for the laser steering and line triggering is presented below. As the original code is highly specialized and functional, the version below is simplified and serves the purpose of giving a bit more insight on how the scanning works.

```
# Inputs
# : v    - speed of galvo scanner
# : dx   - scan distance X axis
# : dy   - scan distance Y axis
# : pix  - number of pixels

# Commands
# : set_jump_speed(linear speed of galvo on image field)
# : jump(move X, move Y, absolute/relative)

set_jump_speed(v)
jump(-dx/2, -dy/2, move_absolute)    # jump to the upper-left corner
for (pix) do:
  trigger_on()
  jump(dx, 0, move_relative)
  trigger_off()
  jump(-dx, dy/pix, move_relative)
```

A.2 Mouse liver swarm imaging

Additional experiment was performed with a 20X objective; result is shown on Fig. A.1(a). Although the image is highly blurred, the algorithm can still identify individual flagella-bots (Fig. A.1(b,c)).

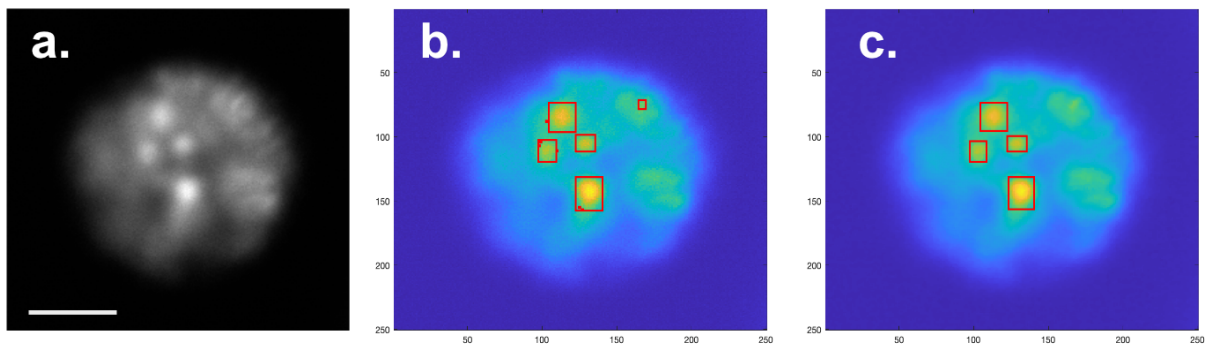


Figure A.1: MPM of the flagella-bots with 20X objective 300 μm inside mouse liver. **a.** Single-frame acquisition of 250×250 image. Scale bar = 50 μm . **b.** Detection algorithm applied on the original image. **c.** Same algorithm applied on image smoothed with median filter.